Cavity Flows in Different Domains and Bifurcation

by

Shunsuke Mizumi

B.Sc. University of Tokyo, 1991.

A THESIS SUBMITTED IN PARTIAL FULFILLMENT
OF THE REQUIREMENTS FOR THE DEGREE OF
MASTER OF SCIENCE
in the Department
of
Mathematics & Statistics

SIMON FRASER UNIVERSITY
July 1995

APPROVAL

Name: Shunsuke Mizumi

Degree: Master of Science

Title of thesis: Cavity Flows in Different Domains and Bifurcation

Examining Committee: Dr. B. R. Alspach
Chair

Dr. T. Tang
Senior Supervisor

Dr. G. A. C. Graham

Dr. M. Trummer

Dr. H. Huang
External Examiner

Date Approved: July 27, 1995

PARTIAL COPYRIGHT LICENSE

I hereby grant to Simon Fraser University the right to lend my thesis, project or extended essay (the title of which is shown below) to users of the Simon Fraser University Library, and to make partial or single copies only for such users or in response to a request from the library of any other university, or other educational institution, on its own behalf or for one of its users. I further agree that permission for multiple copying of this work for scholarly purposes may be granted by me or the Dean of Graduate Studies. It is understood that copying or publication of this work for financial gain shall not be allowed without my written permission.

Title of Thesis/Project/Extended Essay

Cavity Flows in Different Domains and Bifurcation

Author: _____
(signature)

Shunsuke Mizumi
(name)

July 27 '95
(date)

Abstract

The two dimensional flows in a series of differently shaped cavities are investigated. Particular attention is given to flows in right triangular cavities. Some indication of Hopf bifurcation is observed by using the total kinetic energy at relatively large Reynolds number. On the numerical side, the spatial terms of the Navier-Stokes equations are discretized by the finite element method. The second order Gear's type difference method is used to treat time dependent problems.

Dedication

To my wife Chiharu, son Toshiki and daughter Yukino

Acknowledgements

I would like to thank my previous senior supervisor, Dr. Steven Hou, for providing and guiding the direction of the early stage of my research.

I would also like to thank my present senior supervisor Dr. Tao Tang for suggesting to me the present topic and for his patience during the preparation of this thesis.

I have no word to express my appreciation to Dr. G.A.C.Graham for his constant encouragement and for making possible my study at Simon Fraser University.

I owe a great deal to Mr. B.Fulford for correcting my English, Dr. S.S.Ravindran for technical help, and many other friends for emotional help.

Finally, I am deeply grateful to my family and parents for their understanding and constant support in every way.

Contents

List of Tables

List of Figures

Chapter 1

Introduction

Since the dawn of scientific methods like Newtonean mechanics, people have tried to predict natural phenomena either theoretically or experimentally. The theories which describe natural phenomena have been and will be greatly expanded, and have successfully explained many phenomena. On the other hand, industrial experimental models such as wind tunnel have played a very important role in the design of cars, planes and many other things for which wind resistance has to be taken into consideration. However, the difficulties which come from non-linearity or complex geometry make both theoretical and experimental methods virtually impractical in many cases. Until now, in the field of nonlinear problems, only a small number of exceptional cases are completely understood in theory. In addition, when a wind tunnel or like facility are used, a single change of parameters could sometimes mean the reconstruction of the whole actual model which leads to a tremendous amount expenditure of resources and time.

Fortunately a third method, numerical analysis, arose in the late 1940's with the emergence of electronic computers. In many cases, non-linearities can be treated with little difficulty by means of numerical methods. Thanks to the steady improvement in the speed of computers and the memory size in the past few decades, relatively complicated problems such as fluid dynamics have been able to provide analysis to complement theory and experiment cost-effectively. Prior to the late 1960's, the most

widely used computer based numerical methods were the *Method of characteristics* and the *Finite difference method.* Because of its straight-forwardness and ability to handle partial differential equations (PDEs) directly, the finite difference method has been successfully developed and has become very popular. However, this method encounters difficulties in treating problems with complicated domains.

The finite element method (FEM), which was originally developed in the field of solid mechanics, has the great advantage of a capability to handle truly arbitrary geometry. In many powerful industrial codes, very complicated non uniform meshes can be automatically generated and updated so that a certain norm in each element is limited to a fixed value. FEM also has other important features, such as its ability to deal with general boundary conditions and the fact that it can include non homogeneous materials. In other words, we can analyze a system of arbitrary shapes that are constructed with numerous different material regions. With the development of theoretical reasoning and a variety of new algorithms, the use of FEM in Computational Fluid Dynamics (CFD) has rapidly become usual. Modern finite element integral formulations are usually obtained by either of two different procedures; variational formulation or weighted residual formulation. The Ritz method (variational method), which has been well used in stress analysis and structural dynamics is based on minimizing a functional value or seeking the stationary value of a functional. Unfortunately, it is generally difficult or even impossible to find the correct functional corresponding to a PDE. On the other hand, the weighted residual method has many variations including Galerkin's, collocation, least square and subdomain method. Among them, Galerkin's FEM enjoys the greatest popularity, since it can be accommodated to virtually any PDE in a relatively straightforward way.

In chapter 2 we present an overview of the ideas of the FEM procedure: numerical integration, discretization of Navier-Stokes equations and iteration methods for solving systems of equations. The discretization of the time-dependent Navier-Stokes equations is also reviewed briefly. In chapter 3 we present previous work about the steady state cavity flow problems and give some examples of the practical application of triangular cavities. We also show numerical results of steady state driven cavity

flow problems for various shapes from square, through trapezoidal, to triangular domains with relatively low Reynolds numbers. We will study the effect of continuous geometrical change on the physical structure of eddies. One specific case (isosceles right triangle) is further investigated in more detail. In chapter 4 we first review previous work on time-dependent problems including especially bifurcations with incompressible viscous cavity flows. We then consider the time dependent problems for the isosceles right triangle and try to observe the Hopf bifurcation. In chapter 5 we discuss the validity of the results obtained using coarse meshes. Conclusions are presented in chapter 6. In most cases calculated results reasonably match with those of published papers. Throughout this thesis we frequently use Re to indicate Reynolds number for convenience.

Chapter 2

Introduction to the Finite Element Method

The finite element method is a generalization of the classical variational and weighted residual methods which is based on the idea that the solution u of a differential equation can be expressed as a linear combination of basis functions ϕ_j with coefficients u_j. For a weighted residual method, a differential equation will be multiplied by a set of test functions, and then integrated over the domain. The coefficients u_j will be determined so that the differential equation is satisfied in the sense of weak formulation. The basic idea of the finite element method is that the entire domain is considered as a collection of small elements, called finite elements, which can be of different forms such as a triangular or a quadrilateral form and can also be rectilinear or curved.

2.1 linear and quadratic triangular elements

In a PDE, the function value of u will be approximated by a linear combination of polynomials:

$$u \approx \tilde{u}(\underline{x}) = \sum_{j=1}^{N} \tilde{u}(\underline{x}_j)\phi_j(\underline{x})$$

where $\tilde{u}(\underline{x}_j)$ are function values at the points $\underline{x}_j$ and polynomials $\phi_j(\underline{x})$ are basis functions such that :

$$\phi_j = \begin{cases} 1 & : \text{ at j-th node} \\ 0 & : \text{ the rest of the nodes.} \end{cases}$$

2.1.1 linear finite element

For a two-dimensional problem, a piecewise linear basis function ϕ_i, corresponding to nodal point $\underline{x}_i$ is such that:

1. the form of ϕ_i is

$$\phi_i(\underline{x}) = a_1 x + a_2 y + a_3$$

2. the value of ϕ_i is

$$\phi_i(\underline{x}_j) = \delta_{ij} \quad \begin{cases} 1 & : \quad i = j \\ 0 & : \quad i \neq j \end{cases}$$

3. ϕ_i is linear on each e_k

4. ϕ_i is continuous on $\overline{\Omega}$

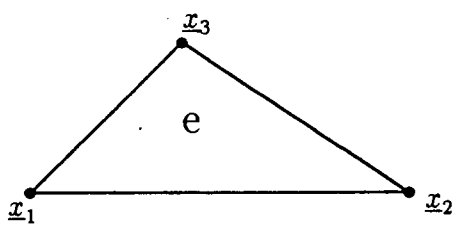

Triangular element e with nodal points $\underline{x}_1, \underline{x}_2, \underline{x}_3$.

We also define the specific linear basis functions $\lambda_1, \lambda_2, \lambda_3$, which allow quadratic basis functions to be written in a compact form:

$$\begin{aligned} \phi_1 &= 1 - \xi - \eta \approx \lambda_1 \\ \phi_2 &= \xi \approx \lambda_2 \\ \phi_3 &= \eta \approx \lambda_3 \end{aligned}$$

where ξ and η are variables in a $\xi \times \eta$ coordinate system.

2.1.2 quadratic finite element

For a two dimensional problem, a piecewise quadratic basis function ϕ can generally be written as

$$\phi(\underline{x}) = a_1x^2 + a_2xy + a_3y^2 + a_4x + a_5y + a_6.$$

Since we have six parameters $(a_1, a_2, \ldots, a_6)$ to be determined, we need six nodes and six corresponding basis functions. They can be expressed by using previously defined $\lambda_i (i = 1, 2, 3)$ as follows:

- for vertices:

$$\phi_i = \lambda_i(2\lambda_i - 1) \quad (i = 1, 2, 3)$$

- for mid points:

$$\phi_{ij} = 4\lambda_i\lambda_j \quad (i, j = 1, 2, 3 \quad i \neq j).$$

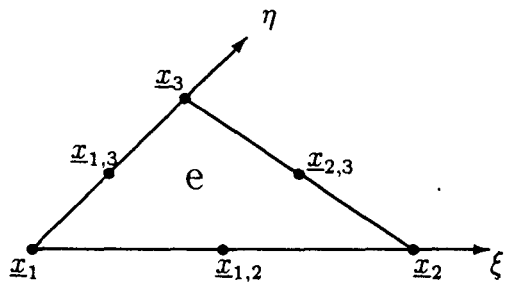

Triangular element e with six nodal points.

• **comment:** Roughly speaking, the use of linear approximating functions produces solutions of about the same accuracy as provided by second-order finite difference methods and the use of quadratic approximating functions generates about the same accuracy as third-order finite difference methods.

2.2 2D Poisson equation and Galerkin formulation

Most of the techniques of the finite element method can be illustrated by the discretization of a Poisson type equation. Let us consider the following problem on a two dimensional region Ω with the boundary Γ.
Find $\mathbf{u}$ such that

$$\begin{aligned} -\nabla^2\mathbf{u} &= \mathrm{f} \quad \text{in} \quad \Omega \\ \mathbf{u} &= 0 \quad \text{on} \quad \Gamma_0 \\ \frac{\partial \mathbf{u}}{\partial \mathbf{n}} &= g_1 \quad \text{on} \quad \Gamma_1 \\ \frac{\partial \mathbf{u}}{\partial \mathbf{n}} + \mathbf{u} &= g_2 \quad \text{on} \quad \Gamma_2 \end{aligned} \tag{2.1}$$

where f, g_1 and g_2 are given functions, $\partial\Omega = \Gamma_0 \cup \Gamma_1 \cup \Gamma_2$. To derive a weak form, we multiply the PDE by an arbitrary test function $\mathbf{v}$ and integrate it over Ω. Then, apply integration by parts or Green's formula to obtain

$$\int\int_\Omega (\nabla\mathbf{u}\cdot\nabla\mathbf{v})d\Omega - \oint_\Gamma \frac{\partial \mathbf{u}}{\partial \mathbf{n}}\mathbf{v}d\Gamma = \int\int_\Omega \mathrm{f}\mathbf{v}d\Omega. \tag{2.2}$$

Now if we choose $\mathbf{v}$ so that $\mathbf{v} = 0$ on Γ_0 (essential condition) and apply boundary conditions to (2.2), the problem becomes:
Find $\mathbf{u}$ such that $\mathbf{u}\,|_{\Gamma_0} = 0$ and

$$\int\int_\Omega \nabla\mathbf{u}\cdot\nabla\mathbf{v}d\Omega + \int_{\Gamma_2} \mathbf{u}\mathbf{v}d\Gamma = \int\int_\Omega \mathrm{f}\mathbf{v}d\Omega + \oint_{\Gamma_1} g_1\mathbf{v}d\Gamma + \int_{\Gamma_2} g_2\mathbf{v}d\Gamma \tag{2.3}$$

for all $\mathbf{v}$ with $\mathbf{v}\,|_{\Gamma_0} \equiv 0$.
To discretize the PDE we substitute the following polynomial into the PDE.

$$\begin{aligned} \tilde{\mathbf{u}}(\underline{x}) &= \sum_{j=1}^{N} \tilde{\mathbf{u}}(\underline{x}_j)\phi_j(\underline{x}) \\ &= \sum_{j=1}^{interior} \tilde{\mathbf{u}}(\underline{x}_j)\phi_j(\underline{x}) + \sum_{j=1}^{exterior} \tilde{\mathbf{u}}(\underline{x}_j)\phi_j(\underline{x}) \end{aligned} \tag{2.4}$$

where $\phi_j(\underline{x})$ are basis functions and $\tilde{\mathbf{u}}(\underline{x}_j)$ are nodal values of the function $\mathbf{u}(\underline{x})$ (N = interior + exterior). Then the PDE together with boundary condition will become:

$$\sum_{k=1}^{K}\sum_{j=1}^{J}\tilde{\mathbf{u}}_j\left\{\int\int_{e_k}\nabla\phi_j\cdot\nabla\phi_i d\Omega\right\}+\sum_{q=1}^{Q}\sum_{j=1}^{J}\tilde{\mathbf{u}}_j\left\{\int_{l_2}\phi_j\phi_i d\Gamma\right\}$$
$$=\sum_{k=1}^{K}\int\int_{e_k}\mathbf{f}\phi_i d\Omega+\sum_{p=1}^{P}\int_{l_1}g_1\phi_i d\Gamma+\sum_{q=1}^{Q}\int_{l_2}g_2\phi_i d\Gamma. \qquad (2.5)$$

Calculation is applied to each subregion and summed up. The subregions e_k are called triangular elements, the subregions l_1, and l_2 are termed line elements. Generally integrals will be calculated in a numerical way.

2.3 Numerical integration

In many cases a definite integral does not have an explicit anti-derivative or the integral is not easily calculated. Therefore, an alternative method to obtain an approximation of the integral is often required. The basic method involved in approximating $\int_a^b f(x)dx$ is called numerical quadrature.

2.3.1 Newton-Cotes method

In this method, points at which the function is to be found are determined priori. The $n+1$ point equally spaced closed Newton-Cotes formula uses nodes $x_i = x_0 + ih$, for $i = 0, 1, \ldots, n$ where $x_0 = a, x_n = b$ and $h = (b-a)/n$. The formula will be

$$\int_a^b f(x)dx \approx \sum_{i=0}^{n} a_i f(x_i)$$

where

$$\begin{aligned} a_i &= \int_{x_0}^{x_n} L_i(x)dx \\ &= \int_{x_0}^{x_n} \Pi_{\substack{j=0 \\ j\neq i}}^{n} \frac{(x-x_j)}{(x_i-x_j)}dx \end{aligned} \qquad (2.6)$$

and $L_i(x)$ is call the ith Lagrange interpolating polynomial.
If $n = 2$ the formula is called Simpson's rule and has the form

$$\int_{x_0}^{x_2} f(x)dx = \frac{h}{3}\left[f(x_0) + f(x_1) + f(x_2)\right]$$

2.3.2 Gaussian quadrature

In this method, instead of choosing equally spaced points, sampling points will be determined so as to obtain the best accuracy. In a manner similar to the Newton-Cotes method, the approximation of a function can be written as

$$\int_a^b f(x) \approx \sum_{i=1}^{n} c_j f(x_j)$$

for an arbitrary function. If we apply the simple linear transformation
$t = [1/(b-a)](2x - a - b)$ to the change of the limits of the integral as

$$\int_a^b f(x)dx = \int_{-1}^{1} f\left(\frac{(b-a)t + b + a}{2}\right)\frac{(b-a)}{2}dt$$

and use following theorem, we can determine the sampling points and the polynomials c_j.

Theorem 1 *If P is any polynomial of degree less than or equal to $2n-1$, then*

$$\int_{-1}^{1} P(x)dx = \sum_{i=1}^{n} c_i P(x_j)$$

where

$$c_i = \int_{-1}^{1} \Pi_{\substack{j=0 \\ j\neq i}}^{n} \frac{(x - x_i)}{(x_i - x_j)}dx$$

and $x_0, x_1, \ldots, x_n$ are the zeros of the nth Legendre polynomial.

In this thesis we used a variation of Gauss quadrature derived by Hammer *et al* [7].

2.4 Finite element error estimate

Here we will state only the main steps for error estimate; the proofs of the corresponding theorems will be omitted.

For a typical elliptic problem satisfying the following conditions

1. $a(\cdot,\cdot)$ is symmetric (not necessary);

2. $a(\cdot,\cdot)$ is continuous:

$$| a(u,v) | \leq \gamma \|u\|_V |v|_V \qquad \text{for all} \quad u, v \in V, \gamma > 0;$$

3. $a(\cdot,\cdot)$ is V elliptic:

$$a(u,v) \geq \alpha \|v\|_V \qquad \text{for all} \quad v \in V, \alpha > 0;$$

4. L is continuous:

$$| L(v) | \leq \Lambda \|v\|_V \qquad \text{for all} \quad v \in V, \Lambda > 0.$$

where V is a Hilbert space with scalar product $(\cdot,\cdot)_V$ and norm $\|\cdot\|_V$, and $a(\cdot,\cdot)$ is a bilinear form and $L(\cdot)$ is a linear functional.

$$\text{If} \qquad u \in V \quad \text{such that:} \quad a(u,v) = L(v) \qquad \text{for all} \quad v \in V,$$

$$\text{and if} \qquad u_h \in V_h \subset V \quad \text{such that:} \quad a(u_h,v) = L(v) \qquad \text{for all} \quad v \in V_h \subset V,$$

then we have the following error estimate:

$$\|u - u_h\|_V \leq \frac{\gamma}{\alpha} \|u - v\|_V \qquad \text{for all} \quad v \in V_h.$$

Now if we simply choose $I^h u$, which is the interpolant of u, as a test function v, then we have

$$\|u - u_h\|_V \leq C \|u - I^h u\|_V \qquad \text{where} \quad u_h \in V_h \subset V, \quad C = \frac{\gamma}{\alpha} > 0.$$

If the domain is divided into simplicial elements, then we can use the following theorem;

$$\|u - I^h u\|_{s,\Omega} \leq Ch^{m-s} \mid u \mid_{m,\Omega}, \quad s \leq m \tag{2.7}$$

And obtain the error estimate for the elliptic problems.

$$\|u - u_h\|_{s,\Omega} \leq Ch^{m-s} \mid u \mid_{m,\Omega}, \quad s \leq m$$

where $\|\cdot\|_s$ is H^s norm, and $|\cdot|_m$ is H^m seminorm.

2.5 Solution method for a system of non-linear equations

2.5.1 Picard iteration

This is one of the simplest methods to handle nonlinearity. The application of this type of method to a highly nonlinear problem such as Navier-Stokes equations leads to a rather slow convergence to the solution. However, it has a reasonably large radius of convergence.
Algorithm for Picard method:

1. Choose initial value u^0
2. For $i = 1, 2, \ldots$ solve:

$$K(\underline{u}^{i-1})\underline{u}^i = \underline{f},$$

   or alternatively

3. For $i = 1, 2, \ldots$ solve :

$$K(\underline{u}^i)\underline{u}^{i-1} = \underline{f}$$

where K is a stiffness matrix for a discrete system, $\underline{f}$ is a vector of force and other known values, and $\underline{u}$ is a vector of unknown variables.

An improvement of convergence rate can sometimes be achieved by using a relaxation formula,

$$K(\underline{u}^{i-1})\underline{u}^* = \underline{f}$$

where

$$\underline{u}^i = \alpha\underline{u}^{i-1} + (1-\alpha)\underline{u}^* \qquad 0 \leq \alpha < 1.$$

For a highly nonlinear problem the use of this method may greatly help to subdue an oscillatory behavior.

2.5.2 Newton's method

As previously mentioned the major drawback of the simple iteration method is its slow convergence. If convergence is not reached within a reasonable number of iterations, we have to apply a faster alternative method. Newton's method is one of the most frequently used quadratically convergent method with relatively small radius of convergence. However, if the current iteration is sufficiently close to the final solution $\overline{u}$, it converges within a few iterations.
For each iteration we look for an approximation $\underline{u}^i$ such that the residual $R(\underline{u}^i)$ of the equation is

$$\begin{aligned} R(\underline{u}^i) &= \underline{f} = K(\underline{u}^{i-1})\underline{u}^{i-1} \\ &= R(\underline{u}^{i-1} + \Delta\underline{u}^i) \\ &\approx 0 \end{aligned} \tag{2.8}$$

This will be rewritten by using a Taylor series expansion in the neighborhood of $\underline{u}^{i-1}$

$$R(\underline{u}^{i-1} + \Delta\underline{u}^i) = R(\underline{u}^{i-1}) + \left[\frac{\partial R}{\partial \underline{u}}\right]_{\underline{u}=\underline{u}^{i-1}} \Delta\underline{u}^i + \cdots = 0$$

Since $\Delta\underline{u}^i = \underline{u}^i - \underline{u}^{i-1}$, this will also be written

$$\left[\frac{\partial R}{\partial \underline{u}}\right]_{\underline{u}=\underline{u}^{i-1}} (\underline{u}^i - \underline{u}^{i-1}) = -R(\underline{u}^{i-1})$$

or

$$\underline{u}^i = \underline{u}^{i-1} - \left[\frac{\partial R}{\partial \underline{u}}\right]^{-1} R(\underline{u}^{i-1}).$$

Since Newton's method is only locally convergent and requires a good initial guess, the data which are produced by a simple iteration method like the Picard method are usually used as starting values. With a good initial guess a small number of iterations is in general sufficient for convergence.

2.5.3 quasi-Newton method

For the equation $R(\underline{u}) = \underline{f} - K(\underline{u})\underline{u}$, Newton's method can be written as

$$\underline{u}^i = \underline{u}^{i-1} - J^{-1}(\underline{u}^{i-1})R(\underline{u}^{i-1})$$

with $J(\underline{u}^{i-1})$ the Jacobian matrix $\partial R(\underline{u}^{i-1})/\partial \underline{u}^{i-1}$. Since the Jacobian matrix has to be calculated in each iteration, this method is very expensive. Instead, in the quasi-Newton method, J will be calculated only every several steps. In contrast to Newton's method, it has a super-linear convergent rate. Engelman *et al* [21] reported that by applying the quasi-Newton method to the Navier-Stokes equations, they obtained a saving of about 50% compared to Newton's method for Re in the range of 100 to 1000, where the initial guess is obtained by one Picard iteration.

2.6 Application of FEM to the Navier-Stokes equations

The governing equations for an incompressible fluid flow are Navier-Stokes equations which expresses the conservation of momentum and the continuity equation which describes the conservation of mass. In the finite element method, there are mainly three methods to discretize those equations; penalty function method, stream function-vorticity method and velocity-pressure method.

2.6.1 stream function-vorticity formulation

Here we explain the stream function-vorticity method briefly. For the incompressible Navier-Stokes equations, we have to treat pressure so that it satisfies the continuity equation. One way to do this is to eliminate the pressure term from the original Navier-Stokes equations.

• Navier-Stokes equations:

$$\frac{\partial u}{\partial t} + u\frac{\partial u}{\partial x} + v\frac{\partial u}{\partial y} = -\frac{\partial p}{\partial x} + \frac{1}{Re}\left(\frac{\partial^2 u}{\partial x^2} + \frac{\partial^2 u}{\partial y^2}\right) \tag{2.9}$$

$$\frac{\partial v}{\partial t} + u\frac{\partial v}{\partial x} + v\frac{\partial v}{\partial y} = -\frac{\partial p}{\partial y} + \frac{1}{Re}\left(\frac{\partial^2 v}{\partial x^2} + \frac{\partial^2 v}{\partial y^2}\right) \tag{2.10}$$

$$\frac{\partial u}{\partial x} + \frac{\partial u}{\partial y} = 0. \tag{2.11}$$

Differentiate equation (2.10) with respect to x and differentiate equation (2.9) with respect to y. Then subtract the latter from the former and get

$$\frac{\partial \omega}{\partial t} + u\frac{\partial \omega}{\partial x} + v\frac{\partial \omega}{\partial y} = \frac{1}{Re}\left(\frac{\partial^2 \omega}{\partial x^2} + \frac{\partial^2 \omega}{\partial y^2}\right) \tag{2.12}$$

where

$$\omega = \frac{\partial v}{\partial x} - \frac{\partial u}{\partial y}. \tag{2.13}$$

Using the stream function Ψ, equation (2.11) is automatically satisfied when the following substitutions are used:

$$u = \frac{\partial \Psi}{\partial y}, \qquad v = -\frac{\partial \Psi}{\partial x}. \tag{2.14}$$

From (2.13) and (2.14), we then have

$$\frac{\partial^2 \Psi}{\partial x_2} + \frac{\partial^2 \Psi}{\partial y^2} = -\omega. \tag{2.15}$$

Also from(2.12) and (2.14), we have:

$$\frac{\partial \omega}{\partial t} + \frac{\partial \Psi}{\partial y}\frac{\partial \omega}{\partial x} - \frac{\partial \Psi}{\partial x}\frac{\partial \omega}{\partial y} = \nu \nabla^2 \omega. \tag{2.16}$$

• finite element discretization

Multiply (2.15) by a test function $\delta\psi$ and (2.16) by a test function $\delta\omega$. Integrating the resulting equations over the domain Ω, we have

$$\int\int_\Omega \delta\psi \nabla^2 \Psi d\Omega + \int\int_\Omega \delta\psi\omega d\Omega = 0 \tag{2.17}$$

$$\int\int_\Omega \delta\omega \frac{\partial\omega}{\partial t} d\Omega + \int\int_\Omega \delta\omega \left(\frac{\partial\Psi}{\partial y}\frac{\partial\omega}{\partial x} - \frac{\partial\Psi}{\partial x}\frac{\partial\omega}{\partial y} \right) d\Omega - \int\int_\Omega \delta\omega\nu\nabla^2\omega d\Omega = 0. \tag{2.18}$$

Integration by parts or Green's formula yields

$$\int\int_\Omega \nabla\delta\psi \cdot \nabla\Psi d\Omega - \int\int_\Omega \delta\psi\omega d\Omega - \int_{\Gamma_s} \delta\psi \frac{\partial\Psi}{\partial n} d\Gamma = 0 \tag{2.19}$$

$$\int\int_\Omega \delta\omega \frac{\partial\omega}{\partial t} d\Omega + \int\int_\Omega \delta\omega \left(\frac{\partial\Psi}{\partial y}\frac{\partial\omega}{\partial x} - \frac{\partial\Psi}{\partial x}\frac{\partial\omega}{\partial y} \right) d\Omega + \int\int_\Omega \nu\nabla\delta\omega \cdot \nabla\omega d\Omega - \int_{\Gamma_x} \nu\delta\omega \frac{\partial\omega}{\partial n} d\Gamma = 0. \tag{2.20}$$

Here the unknowns Ψ, ω and the corresponding first variations $\delta\psi, \delta\omega$ are approximated by using shape functions ϕ_α such as:

$$\Psi = \sum_\alpha \phi_\alpha \Psi(\underline{x}_\alpha), \qquad \delta\psi = \sum_\alpha \phi_\alpha \delta\psi(\underline{x}_\alpha)$$
$$\omega = \sum_\alpha \phi_\alpha \omega(\underline{x}_\alpha), \qquad \delta\omega = \sum_\alpha \phi_\alpha \delta\omega(\underline{x}_\alpha) \tag{2.21}$$

where $\Psi(\underline{x}_\alpha)$ and $\omega(\underline{x}_\alpha)$ are nodal values of the stream function and vorticity, respectively.

2.6.2 velocity-pressure formulation

There are many variations of techniques of this type which treat an instability of this method with high Reynolds number. We will use this method for our calculation.

Start from the Navier-Stokes equations

$$\frac{\partial u}{\partial t} + u\frac{\partial u}{\partial x} + v\frac{\partial u}{\partial y} + \frac{\partial p}{\partial x} - \frac{1}{Re}\nabla^2 u = f_1 \tag{2.22}$$

$$\frac{\partial v}{\partial t} + u\frac{\partial v}{\partial x} + v\frac{\partial v}{\partial y} + \frac{\partial p}{\partial y} - \frac{1}{Re}\nabla^2 v = f_2 \tag{2.23}$$

$$\frac{\partial u}{\partial x} + \frac{\partial u}{\partial y} = 0. \tag{2.24}$$

These equations involve time-dependent terms, linear terms, nonlinear terms and the continuity equation and therefore we consider them separately. We will consider time dependent terms in the later section.

• linear terms :

$$\begin{aligned} -\frac{1}{Re}\nabla^2 u + \frac{\partial p}{\partial x} &= f_1 \\ -\frac{1}{Re}\nabla^2 v + \frac{\partial p}{\partial y} &= f_2 \end{aligned} \tag{2.25}$$

Multiplying both sides of each equation by a test function ϕ and integrate over the domain Ω we get:

$$\begin{aligned} \int_\Omega \left(-\frac{1}{Re}\nabla^2 u + \frac{\partial p}{\partial x}\right)\phi d\Omega &= \int_\Omega f_1 \phi d\Omega \\ \int_\Omega \left(-\frac{1}{Re}\nabla^2 v + \frac{\partial p}{\partial y}\right)\phi d\Omega &= \int_\Omega f_2 \phi d\Omega. \end{aligned} \tag{2.26}$$

We now apply integration by parts (or Green's formula) together with Gauss divergence theorem to obtain

$$\begin{aligned} \int\int_\Omega \left[\frac{1}{Re}\left(\frac{\partial u}{\partial x}\frac{\partial \phi}{\partial x} + \frac{\partial u}{\partial y}\frac{\partial \phi}{\partial y}\right) - p\frac{\partial \phi}{\partial x}\right] d\Omega = \\ \int\int_\Omega f_1 \phi d\Omega + \int_\Gamma \frac{1}{Re}\left(\frac{\partial u}{\partial n}\right)\phi d\Gamma - \int_\Gamma p\phi n_1 d\Gamma \end{aligned} \tag{2.27}$$

$$\begin{aligned} \int\int_\Omega \left[\frac{1}{Re}\left(\frac{\partial v}{\partial x}\frac{\partial \phi}{\partial x} + \frac{\partial v}{\partial y}\frac{\partial \phi}{\partial y}\right) - p\frac{\partial \phi}{\partial y}\right] d\Omega = \\ \int\int_\Omega f_2 \phi d\Omega + \int_\Gamma \frac{1}{Re}\left(\frac{\partial v}{\partial n}\right)\phi d\Gamma - \int_\Gamma p\phi n_2 d\Gamma. \end{aligned} \tag{2.28}$$

Seek an approximate solution of the form;

$$\begin{aligned} u \approx \tilde{u} &= u_0 + \sum_{j=1}^{N} u_j \phi_j(\underline{x}) \\ v \approx \tilde{v} &= v_0 + \sum_{j=1}^{N} v_j \phi_j(\underline{x}) \\ p \approx \tilde{p} &= \sum_{j=1}^{M} p_j \psi_j(\underline{x}). \end{aligned} \tag{2.29}$$

where u_0 and v_0 satisfy the Dirichlet boundary condition and $\phi_j(\underline{x})$ and $\psi_j(\underline{x})$ take value zero on the boundaries. Then the equation (2.27) and (2.28) can be compactly written as:

$$\begin{aligned} \int\int_\Omega \frac{1}{Re}\nabla\tilde{u}\cdot\nabla\phi d\Omega - \int\int_\Omega \tilde{p}\frac{\partial\phi}{\partial x}d\Omega &= \int\int_\Omega f_1\phi d\Omega \\ \int\int_\Omega \frac{1}{Re}\nabla\tilde{v}\cdot\nabla\phi d\Omega - \int\int_\Omega \tilde{p}\frac{\partial\phi}{\partial y}d\Omega &= \int\int_\Omega f_2\phi d\Omega. \end{aligned} \tag{2.30}$$

• nonlinear terms (Incremental method or Newton like method) :

If the nth iteration $\underline{u}^n$ is close to the solution u, then the error δu will be small. Thus for each iteration of this method, nonlinear terms can be written as;

$$\begin{aligned} \underline{u}^n\cdot\nabla\underline{u}^n &= (\underline{u}^{n-1}+\delta\underline{u}^{n-1})\cdot\nabla(\underline{u}^{n-1}+\delta\underline{u}^{n-1}) \\ &= \underline{u}^{n-1}\cdot\nabla\underline{u}^n + \underline{u}^n\cdot\nabla\underline{u}^{n-1} - \underline{u}^{n-1}\cdot\nabla\underline{u}^{n-1} + \delta\underline{u}^{n-1}\cdot\nabla\delta\underline{u}^{n-1} \\ &\approx \underline{u}^{n-1}\cdot\nabla\underline{u}^n + \underline{u}^n\cdot\nabla\underline{u}^{n-1} - \underline{u}^{n-1}\cdot\nabla\underline{u}^{n-1}. \end{aligned} \tag{2.31}$$

Therefore the integrated form will be:

$$\int\int_\Omega \left(\underline{u}^n\cdot\nabla\underline{u}^{n-1} + \underline{u}^{n-1}\cdot\nabla\underline{u}^n\right)\phi d\Omega - \int\int_\Omega \left(\underline{u}^{n-1}\cdot\nabla\underline{u}^{n-1}\right)\phi d\Omega$$

or more explicitly

$$\begin{aligned} &\int\int_\Omega \left(u^n\frac{\partial u^{n-1}}{\partial x} + v^n\frac{\partial u^{n-1}}{\partial y} + u^{n-1}\frac{\partial u^n}{\partial x} + v^{n-1}\frac{\partial u^n}{\partial y}\right)\phi d\Omega \\ &\qquad - \int\int_\Omega \left(u^{n-1}\frac{\partial u^{n-1}}{\partial x} + v^{n-1}\frac{\partial u^{n-1}}{\partial y}\right)\phi d\Omega \end{aligned} \tag{2.32}$$

$$\begin{aligned} &\int\int_\Omega \left(u^n\frac{\partial v^{n-1}}{\partial x} + v^n\frac{\partial v^{n-1}}{\partial y} + u^{n-1}\frac{\partial v^n}{\partial x} + v^{n-1}\frac{\partial v^n}{\partial y}\right)\phi d\Omega \\ &\qquad - \int\int_\Omega \left(u^{n-1}\frac{\partial v^{n-1}}{\partial x} + v^{n-1}\frac{\partial v^{n-1}}{\partial y}\right)\phi d\Omega \end{aligned} \tag{2.33}$$

Since Newton's method is only a locally convergent method, we used a simple iteration method for the first few steps. In other words, convection terms $u^n(\nabla\cdot u^n)$ will be approximated by $u^n(\nabla\cdot u^{n-1})$. In general, by carefully choosing an initial data, only a small number of iterations is required for the solution to converge. Furthermore,

Engelman *et al* [21] reported that for Navier-Stokes problems, the result of one Picard iteration is usually a good starting value for the Newton process. This method is fully explained in [1].

•continuity equation:

For the continuity equation we will use the integrated form as follows:

$$\int\int_{\Omega}\left(\frac{\partial u^n}{\partial x}+\frac{\partial v^n}{\partial y}\right)\psi d\Omega = 0.$$

•Comment: By Glowinski and Pironneau [8], and Bercovier and Pironneau [9], it is found that if the pressure is included in a Galerkin formulation, the optimal convergence is obtained if the pressure shape function is one order lower than the velocity shape function.

2.6.3 the penalty function method

In the penalty function method, the continuity equation is perturbed and the pressure term is eliminated. The main advantage over the integrated method is the considerable reduction of both memory and computation time required. However, the physical meaning of the penalty term is still uncertain.

Here we only consider the Stokes equation, since the Navier-Stokes equations can be treated in a similar manner:

$$-\frac{1}{Re}\nabla^2 u+\frac{\partial p}{\partial x} = f_1 \quad \text{in} \quad \Omega \tag{2.34}$$

$$-\frac{1}{Re}\nabla^2 v+\frac{\partial p}{\partial y} = f_2 \quad \text{in} \quad \Omega \tag{2.35}$$

$$\frac{\partial u}{\partial x}+\frac{\partial v}{\partial y} = 0 \quad \text{in} \quad \Omega \tag{2.36}$$

where $\underline{u} = 0$ on Γ, the boundary of Ω. The idea of the penalty function method is to perturb the continuity equation with a small term containing the pressure:

$$\varepsilon p + \nabla \cdot \underline{u} = 0$$

or

$$p = -\tau \nabla \cdot \underline{u} \quad (\tau = 1/\varepsilon) \tag{2.37}$$

with ε a small parameter. Now the solution for velocity and pressure will be approximated by shape functions ϕ_j, ψ_j respectively. To satisfy a continuity equation properly, the degree of ϕ_j should be one higher than that of ψ_j.

$$u \approx \tilde{u} = \sum_{j=1}^{N} u_j \phi_j(\underline{x}) = \underline{\phi}^T \underline{u} \tag{2.38}$$

$$v \approx \tilde{v} = \sum_{j=1}^{N} v_j \phi_j(\underline{x}) = \underline{\phi}^T \underline{v} \tag{2.39}$$

$$p \approx \tilde{p} = \sum_{k=1}^{M} p_k \psi_k(\underline{x}) = \underline{\psi}^T \underline{p} \tag{2.40}$$

where $\underline{\phi}$ and $\underline{\psi}$ are (column) vectors of interpolation (or shape) functions, and vectors $\underline{u}, \underline{v}$ and $\underline{p}$ are nodal values of velocity components and pressure, respectively.

The discretized form of the penalty function formulation will be

$$\int\int_\Omega \frac{1}{Re} \nabla \tilde{u} \cdot \nabla \phi_i d\Omega - \int\int_\Omega \tilde{p} \frac{\partial \phi_i}{\partial x} d\Omega = \int\int_\Omega f_1 \phi_i d\Omega \tag{2.41}$$

$$\int\int_\Omega \frac{1}{Re} \nabla \tilde{v} \cdot \nabla \phi_i d\Omega - \int\int_\Omega \tilde{p} \frac{\partial \phi_i}{\partial y} d\Omega = \int\int_\Omega f_2 \phi_i d\Omega \tag{2.42}$$

where $i = 1, 2, \ldots, N$, and

$$\int\int_\Omega \tilde{p} \psi_k d\Omega = -\tau \int\int_\Omega \psi_k \left(\frac{\partial \tilde{u}}{\partial x} + \frac{\partial \tilde{v}}{\partial y} \right) d\Omega \tag{2.43}$$

where $k = 1, 2, \ldots, M$. By substituting (2.40) into (2.43), a simple manipulation of (2.43) will allow us to express pressure vector $\underline{p}$ as:

$$\underline{p} = -\tau \left[\int\int_\Omega \phi_j \phi_i d\Omega \right]^{-1} \left[\int\int_\Omega \psi_k \left(\frac{\partial \tilde{u}}{\partial x} + \frac{\partial \tilde{v}}{\partial y} \right) d\Omega \right] \tag{2.44}$$

where $[\ ]^{-1}$ indicates the inverse of the matrix. From (2.41) and (2.42) we can eliminate the pressure to obtain uncoupled equations in a compact matrix vector notation:

$$S\underline{u} + \tau L^T D^{-1} L \underline{u} = \underline{F} \tag{2.45}$$

where

$$S = \int\int_\Omega \frac{1}{Re} \nabla \phi_i \cdot \nabla \phi_j d\Omega$$

$$L = \int\int_\Omega \psi_i \frac{\partial \phi_j}{\partial x_k} d\Omega \qquad k = 1, 2 \quad x_1 = x \quad x_2 = y$$

$$D = \int\int_{\Omega} \psi_i \psi_j d\Omega$$
$$\underline{F} = \int\int_{\Omega} f_k \phi_i d\Omega \qquad k = 1, 2. \tag{2.46}$$

The main advantage of this construction is that the computation of the velocity and pressure are uncoupled. First the velocity $\underline{u}$ and $\underline{v}$ are computed from (2.45) then the pressure is computed separately from (2.44).

• **Comment**: In theory the pressure satisfying the Navier-Stokes equation can only be determined up to an additive constant. One way to determine the pressure is to claim that:

$$\int\int_{\Omega} p d\Omega = 0.$$

In numerical computation, for the sake of simplicity, the pressure is usually prescribed at one point. That is we set

$$\tilde{p}(\underline{x}) = p_0 + \sum_{j=1}^{M-1} p_j \phi_j(\underline{x})$$

with p_0 the additive constant.

2.7 Time-dependent problems for FEM

There are many ways to discretize the time-dependent part. One way to do this, is to apply Galerkin's method to the time direction. But this is not popular. Instead, we will present some different ways which are commonly used to discretize the time-dependent part. Since after applying Galerkin's method to spatial terms, a partial differential equation (PDE) becomes an ordinary differential equation (ODE), we can basically apply any methods which have been developed to solve ODEs.

2.7.1 finite difference in time

• Some examples of the finite difference approximation of the time-dependent part of $\partial u/\partial t$ are:

$$\begin{aligned}
\frac{\partial u}{\partial t} &= \frac{u^{i+1}-u^{i}}{\Delta t}+O(\Delta t)\\
\frac{\partial u}{\partial t} &= \frac{u^{i}-u^{i-1}}{\Delta t}+O(\Delta t)\\
\frac{\partial u}{\partial t} &= \frac{u^{i+1}-u^{i-1}}{\Delta t}+O(\Delta t^2)\\
\frac{\partial u}{\partial t} &= \frac{-u^{i+2}+4u^{i+1}-3u^{i}}{2\Delta t}+O(\Delta t^2)\\
\frac{\partial u}{\partial t} &= \frac{3u^{i}-4u^{i-1}-u^{i-2}}{2\Delta t}+O(\Delta t^2).
\end{aligned}$$

• The θ method:

After the discretization, the Navier-Stokes equations will be reduced to a system of ordinary differential equations of the form

$$\dot{\underline{u}} = F(\underline{u}, t) \tag{2.47}$$

with initial condition $\underline{u}(0) = \underline{u}^0$. The θ method applied to (2.47) is:

$$\frac{\underline{u}^{n+1}-\underline{u}^{n}}{\Delta t} = \theta F(\underline{u}^{n+1}, t^{n+1}) + (1-\theta)F(\underline{u}^{n}, t^{n}), \qquad 0 \le \theta \le 1 \tag{2.48}$$

where t^n denotes the nth time level and $\underline{u}^n$ the solution of (2.48). Special cases of the θ method are:

- $\theta = 0$ (explicit Euler scheme):

$$\frac{\underline{u}^{n+1}-\underline{u}^{n}}{\Delta t} = F(\underline{u}^{n}, t^{n}) + O(\Delta t)$$

- $\theta = 1/2$ (Crank-Nicolson scheme):

$$\frac{\underline{u}^{n+1}-\underline{u}^{n}}{\Delta t} = \frac{1}{2}\left[F(\underline{u}^{n+1}, t^{n+1}) + \frac{1}{2}F(\underline{u}^{n}, t^{n})\right] + O(\Delta t^2)$$

- $\theta = 1$ (implicit Euler scheme):

$$\frac{\underline{u}^{n+1} - \underline{u}^n}{\Delta t} = F(\underline{u}^{n+1}, t^{n+1}) + O(\Delta t)$$

In the case of nonlinear problems, after the discretization of the spatial terms the PDE becomes a nonlinear ODE, and we can apply any ODE methods to obtain numerical solutions. In practice, predictor-corrector type algorithms such as the Adams-Bashforth method or Runge-Kutta type schemes are also popular. For the comprehensive discussion of the theoretical aspect of the time-dependent FEM, see references [34, 35, 36].

2.7.2 application of θ method to NS equations

Most of the processes to discretize the time-dependent Navier-Stokes equations are the same as the steady state case. For the sake of brevity, we start from the simplified form of the equations.

$$M\dot{\underline{u}} + S\underline{u} + N(\underline{u})\underline{u} + L^T\underline{p} = \underline{F} \tag{2.49}$$

$$L\underline{u} = 0 \tag{2.50}$$

$$\underline{u}(0) = \underline{u}_0 \tag{2.51}$$

where in two dimensions

$$\begin{aligned}
S &= \int\int_\Omega \frac{1}{Re}\nabla\phi_i \cdot \nabla\phi_j d\Omega \\
N_{u_k u_k} &= \int\int_\Omega \left(\phi_j \frac{\partial u_k^{n-1}}{\partial x_k} + u^{n-1}\frac{\partial \phi_j}{\partial x} + v^{n-1}\frac{\partial \phi_j}{\partial y}\right)\phi_i d\Omega \\
N_{u_k u_l} &= \int\int_\Omega \phi_j \frac{\partial u_k^{n-1}}{\partial x_l}\phi_i d\Omega \\
L &= \int\int_\Omega \psi_i \frac{\partial \phi_j}{\partial x_k} d\Omega \qquad k = 1,2 \quad x_1 = x \quad x_2 = y \\
\underline{F} &= \int\int_\Omega f_k \phi_i d\Omega \qquad k = 1,2.
\end{aligned} \tag{2.52}$$

After the application of previously presented θ method to (2.49), we obtain

$$M\frac{\underline{u}^{n+1}-\underline{u}^{n}}{\Delta t}+S\left[\theta\underline{u}^{n+1}+(1-\theta)\underline{u}^{n}\right]+\theta N(\underline{u}^{n+1})\underline{u}^{n+1}+(1-\theta)N(\underline{u}^{n})\underline{u}^{n}$$
$$+L^{T}\left[\theta\underline{p}^{n+1}-(1-\theta)\underline{p}^{n}\right]=\theta\underline{F}^{n+1}+(1-\theta)\underline{F}^{n}, \tag{2.53}$$
$$L\underline{u}^{n+1}=0. \tag{2.54}$$

Since (2.53) has exactly the same structure as the system of equations for the steady state Navier-Stokes equations, we may be able to apply the same linearization techniques as the nonlinear steady state problems. Unlike the stationary case, we do not usually need any iteration to solve the nonlinear equations. For Δt small enough the difference between two succeeding time-steps is small and the preceding time-step gives a sufficient initial guess for the linearization method. Application of Newton linearization to (2.53) will produce:

$$(M+\theta\Delta tS)\underline{u}^{n+1}+\theta\Delta tN(\underline{u}^{n+1})\underline{u}^{n}+\theta\Delta tN(\underline{u}^{n})\underline{u}^{n+1}+\theta\Delta tL^{T}\underline{p}^{n+1}$$
$$=(M-(1-\theta)\Delta t(S+N(\underline{u}^{n})))\underline{u}^{n}-(1-\theta)\Delta tL^{T}\underline{p}^{n}$$
$$+\theta\Delta tN(\underline{u}^{n})\underline{u}^{n}+\theta\Delta t\underline{F}^{n+1}+(1-\theta)\Delta t\underline{F}^{n}. \tag{2.55}$$

The Crank-Nicolson scheme ($\theta=\frac{1}{2}$) is the most accurate one for solutions in time. For non-smooth solutions in space, Crank-Nicolson may cause numerical oscillations when large time steps are used. In that case $\theta > 0.5$ should be used, for example $\theta = 0.75$ or $\theta = 1$.

Chapter 3

Steady flows in different cavity shapes

Steady viscous flows in a variety of shapes of the domains from trapezoids, through the square, to triangles are investigated. The Navier-Stokes equations are solved numerically using the Galerkin finite element method. The results show a primary eddy and a secondary eddy at the stagnant corner of most of the shapes with large Reynolds number. We first present some published works on cavity flow problems. Then we will present the results in several different shape patterns with a fixed Reynolds number Re=1000. The main aim of this chapter is to discuss the physical effect of the shape-chang to the properties of the physical structure of eddies.

3.1 review of cavity flow problems

Even though the power of computers has been greatly increased in both speed and memory storage, the calculation of highly nonlinear, time-dependent, three dimensional or complicated geometric problems is still a big task: On the other hand, many real life applications involve relatively simple shapes or repetition of simple shapes. Thus relatively simple problems such as a steady incompressible viscous flow within

a rectangular cavity are still very important in computational fluid dynamics both in their own right as physical phenomena and for engineering applications. Because of their simple closed geometry, the problems have also been used as computationally important model problems for testing and evaluating numerical techniques. As we can easily guess, the two dimensional square viscous cavity flow with three non-slip walls and a top lid moving at a constant speed has been the most widely studied case in the literature of numerical computation. For the investigation of this cavity flow, a number of schemes have been applied; finite difference, spectral method, multigrid method, finite element method, etc. (see references [13, 15, 16, 28, 30]).

Although the square cavity flow problem is regarded as essentially solved, there are still some minor differences in the numerical results. For example, the results of a small vortex at the upstream of the top lid are not consistent for all researchers nor even observed experimentally (see [10] and its references). Quere and Roquefort [16] solved the classical problem of natural convection of a Boussinesq fluid in square and rectangular cavities by using a semi-implicit spectral method with Rayleigh number up to 10^7. Kim and Moin [30] used a square driven cavity flow as a test case for evaluating the stability and accuracy of their fractional-step method before applying it to three dimensional backward-facing step problem. Ghia *et al* [28] studied a square cavity flow with high resolution grid (257×257) for Reynolds number up to 10,000 by using multigrid method. Since the calculation is done with very high resolution, their results are often used as benchmark results. Tuam and Olson [13] reviewed and categorized computational methods for recirculating flows in the relatively early days (1978) of the development of the computational fluid dynamics. They mentioned that in many cases, the FEM appeared to be the most accurate and stable for the same number of unknowns. This, however, took no account of computing effort and time which may be higher or lower. In 1986 Gustafson and Halasi [15] tabulated the works done on a rectangular cavity and further investigated the vortex dynamics of rectangular cavity flows with several aspect ratios. They calculated the unsteady driven cavity flow by the MAC method with particular attention to the formulation and evolution of vortices and eddies. The next chapter is related to their work.

Cavity flow problems in a relatively simpler geometry than square are rarely investigated in the literature of fluid dynamics. Triangular or rectangular shapes are, in fact, as common as the square in practice. For the design of fluid flow across corrugated boundaries, the study of triangular groove is extremely important. As mentioned in [10, 11], triangular and trapezoidal grooves, which are wider at opening, are easier to mill than square one. For another example, Sparrow and Charmchi [17] studied analytically and numerically the laminar flow and heat transfer in corrugated-wall ducts. Their work aimed to evaluate and enhance the heat transfer efficiency of an air-operated solar collector compared to other shapes such as parallel-wall channel. Another example for the application of the triangular cavity is studied by Savvides and Gerrard [18]. Steady and unsteady incompressible flows through a periodically corrugated tube are investigated by a finite difference method with the stream function-vorticity formulation. As a medical application of the triangular cavity flow model, arterial prostheses was cited. For the treatment of arteriosclerosis, the most effective way is to bypass the obstructed artery. When no patient's own vein is available a prosthetic artery must be used, and many of these have corrugated walls, so that they remain open when bent. In the design of corrugated artery tube, the effect of the size change of the corrugations is important since it may cause local stasis which promotes the formulation of thrombus. This provides motivation for our computation.

Recently, Ribbens *et al* [10, 11] studied the physical structure of steady viscous flows in triangular and rectangular cavities by a finite difference method using transformed geometry. Their method is based on a fourth-order streamfunction formulation. An arbitrary triangle is transformed to the isosceles right triangle with a special numerical treatment in the corners. They pointed out the failure of the direct application of the algorithms developed in Schreiber and Keller [14]. Li and Tang [12] proposed an alternative approach based on the Navier-Stokes equations in terms of the streamfunction-vorticity formulation, which appeared to be more efficient than those based on the fourth-order streamfunction formulation. With the help of a special

linear transformation mapping, the former formulation can treat an arbitrary triangular shape. Schreiber and Keller [33] indicated that computational results obtained by an insufficiently fine grid might be spurious, inferring a lot of earlier numerical calculations may be erroneous.

Less work has been done for geometries more complicated than rectangular or triangular cavities. Invention of numerical schemes for such problems, especially using finite differences, is an on-going and important activity [19, 20]. Moreover, many authors use a uniform grid for which efficient algorithms are available, despite the fact that a huge number of unknowns are involved for high Reynolds numbers. In our calculation non-uniform grids are used for some of the shapes in order to obtain a convergent solution with a reasonable number of unknowns and iterations.

3.2 numerical results

In the programing of FEM the procedure is usually divided into several parts; parameter input, mesh generation, boundary condition, assembly, linear system solver and data output. To solve the matrix system we used a direct method, namely banded Gaussian elimination. Therefore computational time is generally governed by the linear system solver part. If we double the number of grid lines, the grid points will be quadrupled and band width will be doubled. Thus the resulting system will be at least eight times more expensive. In the case of 55×55 grid (1540 points) for right triangular cavity, it requires about 70 minutes CPU time. For one iteration this seems to be the maximum acceptable time with our UNIX work station.

For the non-uniform grid simple *sine* mapping is employed, which seems to be well suited to mend the corner singularity. Although we used rather coarse grids (about 1000 grid points) for most of the calculation, we can see graphically that they still hold essential properties compared with published results (see [10, 11, 12]). Throughout this chapter the Reynolds number for most of the figures shown is fixed to 1000, and the meshes used are 33×33 grid (1089 points) for the square cavity, 67×23 grid (1035

points) for the trapezoidal cavities, 45×45 grid (1035 points) for the right triangular cavities and 65×33 grid (1089 points) for the other triangular cavities. Since we used the same magnification of the velocities for all computed figures, the vortex composed of short vectors should represent for a vortex rotating at a slower speed than those with longer arrows.

We calculated with many different Reynolds number for all figures (most of them are not presented) and observed that basic global phenomena for all shapes seem to be common: the primary eddy first moves toward downstream wall then bounced back towards the upstream in all cases and towards the middle of the domain, especially with axisymmetric shapes. Up to Re=1000, the shapes of eddies generally tend to be a complete circle with higher Re. Moreover, as Re increases the size of eddies becomes larger and the center moves downwards followed by the emergence of a secondary eddy. For Re=1 the velocity fields for axisymmetric geometries are almost symmetric with respect to the line x=0.5. We found that for a square cavity it is easier to increase the Reynolds number than for any other shapes. Isosceles right triangles with negative directional wind are the most difficult cavity shape for which to obtain convergence. This, I think, is because the most of the flow energe has to be compressed into a small area.

We will now begin to see results with Figure 3.1. We first considered the effect of constant change of the ratio of the moving top lid to the bottom wall. In this sense the last two smaller triangular figures are different from other six, but they can still be obtained from the continuous transformation of the previous triangle. As we can expect, figures with wider moving wall tend to have larger eddy. Since our coarse grids do not have sufficient resolutions, we graphically determined the center of primary eddies instead of using the computed numerical values. However, this should still help us to show the essential movement of primary eddies. For most of the cases Newton-like iteration methods converged to the error of the residuals within 10^{-6} at four to six iterations for Re up to 1000 with increment of ΔRe=200.

In pattern 2 (see Figure 3.3), the effect of a change of the bottom wall is considered. Although Figure 3.3-(a) is quantitatively distinct from other four, it is observed that

Table 3.1: Center of the eddy for equilateral triangular cavity flows. Co-Re stands for conventional Reynolds number

Re		x coordinate	y coordinate
Re=50 (Co-Re=173)	Li and Tang (h=1/80)	0.606	0.704
	McQuain *et al* (h=1/200)	0.599	0.706
	our result (h=1/45)	0.606	0.697
Re=100 (Co-Re=346)	Li and Tang (h=1/80)	0.606	0.682
	McQuain *et al* (h=1/200)	0.595	0.680
	our result (h=1/45)	0.606	0.685
Re=200 (Co-Re=693)	Li and Tang (h=1/80)	0.550	0.650
	McQuain *et al* (h=1/200)	0.560	0.658
	our result (h=1/45)	0.581	0.661

the basic flow properties are common to all figures. There is a relatively large eddy around the center of the domain and a counter-rotating secondary eddy near the bottom right corner. We can also recognize that at least the size of primary eddies is very sensitive to an angle of the corner at downstream (see for example Figure 3.3-(a)). Comparing the figures with negative and positive wind, latter cases have relatively larger primary eddies with a perfectly round circle. The bottom right chart explains the transition of the shapes which is equivalent to the figure pattern we used. To save coding time, we introduced geometries with negative wind direction (goes left) although we originally meant to use geometries with only positive wind direction (goes right). In this thesis all the figures with negative wind should have corresponding figures with positive wind which produce the essentially same results.

The geometries in Figure 3.4 except for right triangles are investigated by McQuan *et al* [10, 11] with the fourth order stream function formulation, and by Li and Tang [12] with the second order stream function-vorticity formulation. Since they used $2\sqrt{3}$-fold for Re, we can not exactly compare the results with presented figures. We, instead, give the comparison of center of eddies for only three different cases (see Table 3.1). For example, conventional Re=1000 should mean Re=289 for their $2\sqrt{3}$- fold Re. Basic flow structures and the center of the primary eddies are quite well matched

to those in [10, 11, 12]. We can clearly see from Figure 3.4 that the primary eddy becomes large and is pushing the secondary eddy toward the bottom right corner as shapes change.

In Figure 3.5 figures on the left correspond to positive wind direction and figures on the right correspond to negative wind direction, it is much harder to increase the Reynolds number for the figures on the right. For the left hand geometries we could increase Re up to 4800 with little difficulty by using 53×53 grid (1540 points). It seems that for right hand figures the primary eddy has to be squeezed into the small corner which has stronger singularity. Moreover it also seems that the eddies tend to retain a circle, but the right hand side figures seem to have difficulty in forming a completely round eddy.

Here we will see a specific shape (Figure 3.6), the isosceles triangular with negative wind direction. From x-directional velocity profile (right bottom), we can see that the secondary eddy is clearly formulated at Re=1000 though there is already a sign of the secondary eddy at Re=500. As Reynolds number increases the primary eddy quickly moves towards upper left corner and the size becomes smaller to leave large enough space for secondary vortex to generate. At Re=3000 we can observe that the small tertiary eddy begins to appear between the primary and the secondary eddies. By this mesh we can easily increase Re up to 2000 with increment size ΔRe=200. However, after about 2000 we have to use smaller increment such as ΔR=50 and we could not obtained convergent solution for Re higher than 3440 with this mesh.

Overall, though we did not use the same type of mesh for each case and it is not easy to make conclusions, we still have feeling that the problems with negative wind direction seems to be harder to converge. In other words, the problems in which wind goes to narrower corner (such as Figure 3.6) require more steps to converge than the problem in which wind goes to the corner with wider angle.

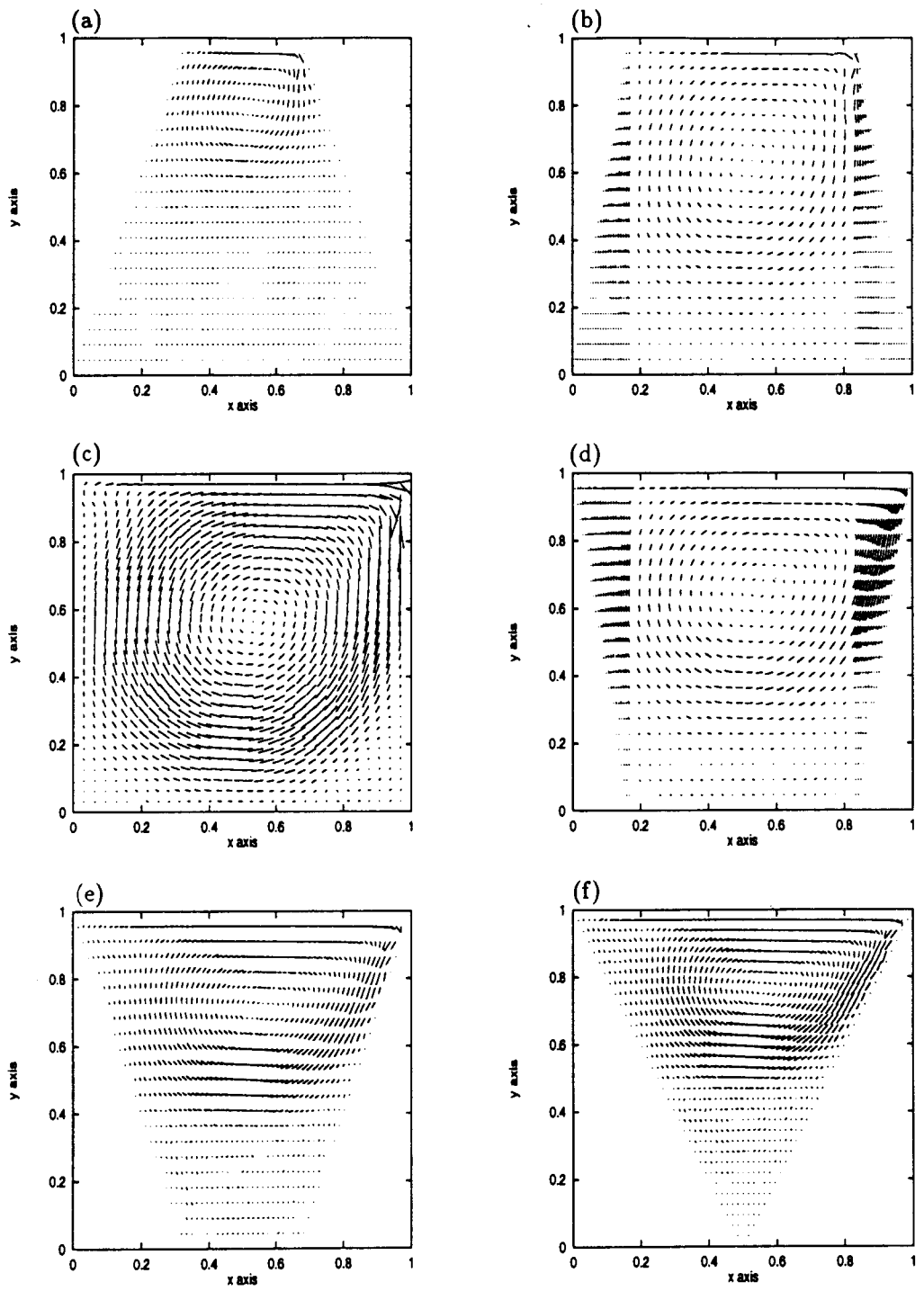
(a)
(b)
(c)
(d)
(e)
(f)
y axis
x axis
0
0.2
0.4
0.6
0.8
1

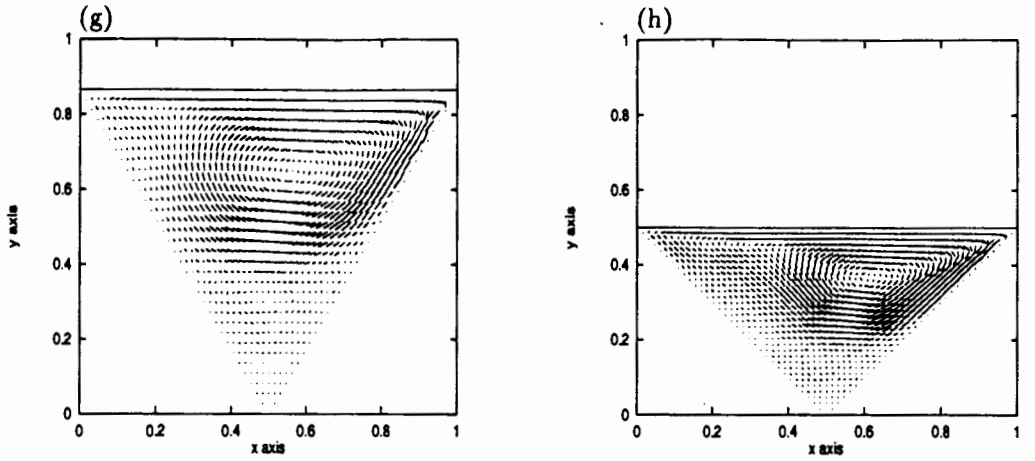

Figure 3.1: Transition of the shape pattern 1.
Re=1000 and wind goes x-positive direction for all figures.
(a) trapezoid → (b) trapezoid 2 → (c) square → (d) trapezoid 3 →
(e) trapezoid 4 → (f) triangle 1 → (g) triangle 2 → (h) triangle 3.

Table 3.2: Center of the eddy for symmetrical cavity flows

figure	fig a	fig b	fig c	fig d	fig e	fig f	fig g	fig h
x axis	0.51	0.56	0.53	0.58	0.56	0.56	0.56	0.62
y axis	0.77	0.66	0.56	0.66	0.72	0.76	0.64 (0.74%)	0.36 (65%)

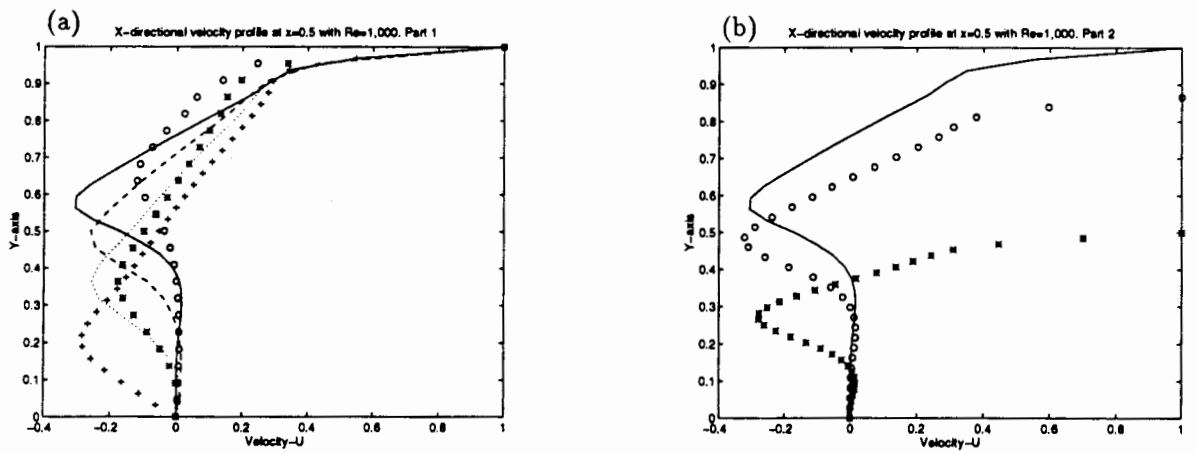

Figure 3.2: X-directional velocity profiles at x=0.5 with Re=1000
Figure (a) to (f) for the left hand side plot and figure (f) to (h) for the right hand side plot.

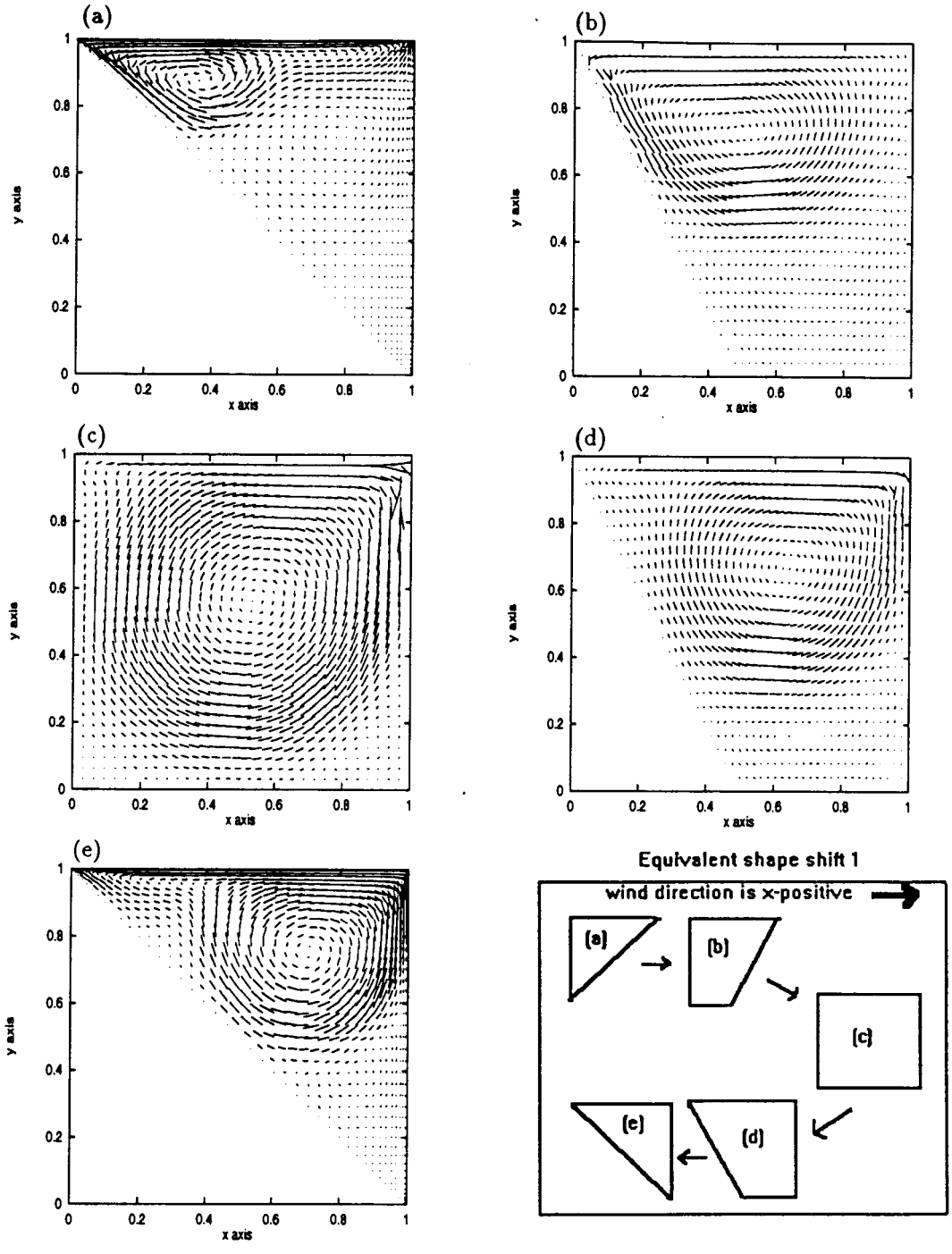

Figure 3.3: Transition of the shape pattern 2.
(a) right triangle 1 (top left) → (b) trapezoid 1 → (c) square → (d) trapezoid 2 → (e) right triangle 2.
For the figure (a) and (b) wind goes x-positive direction and
for the rest of the figures, wind goes x-negative direction.

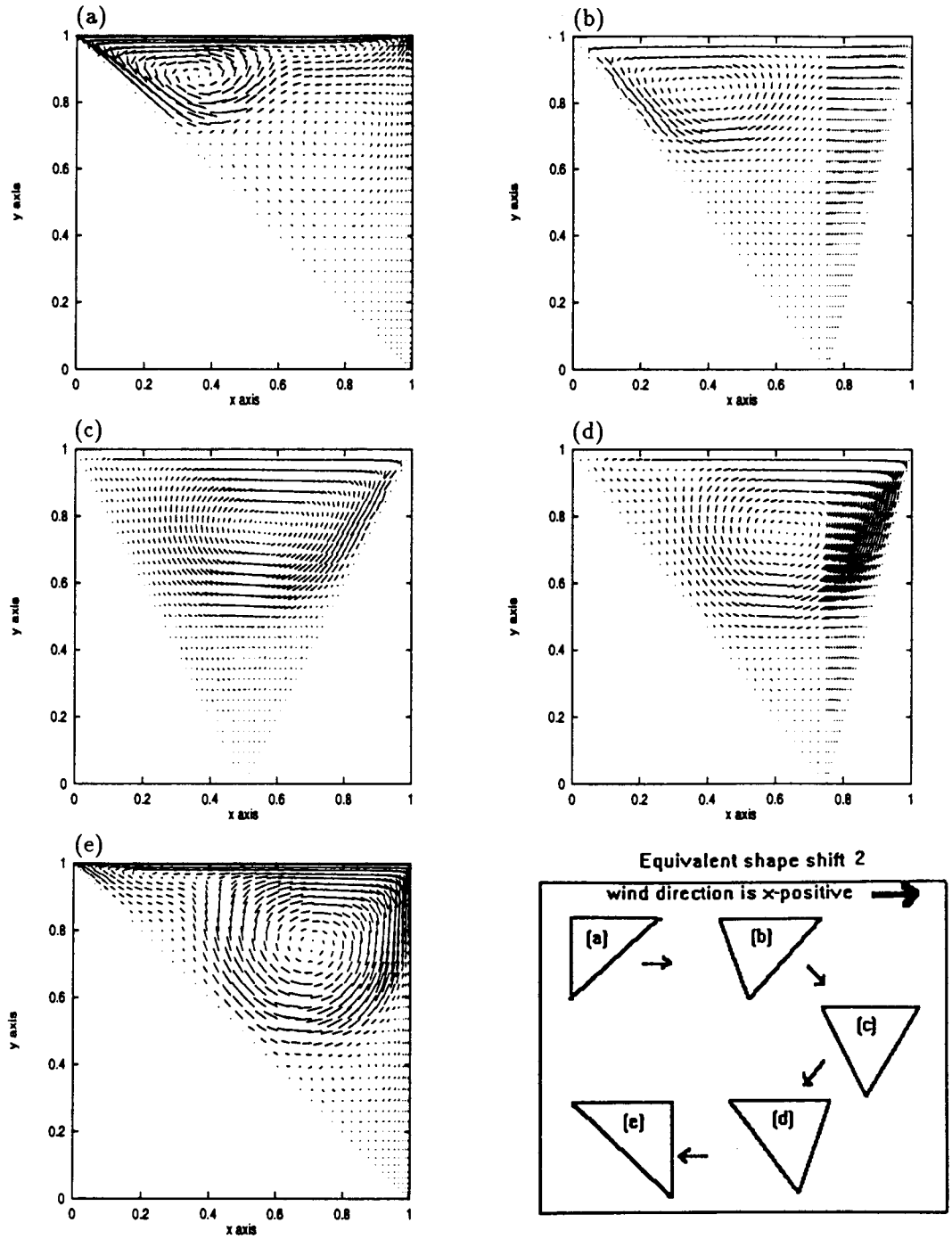

Figure 3.4: Transition of the shape pattern 3.
(a) right triangle 1 (top left) → (b) triangle 1 → (c) triangle 2 → (d) triangle 3 → (e) right triangle 2.
For the figure (a) and (b) wind goes x-positive direction and
for the rest of the figures, wind goes x-negative direction.

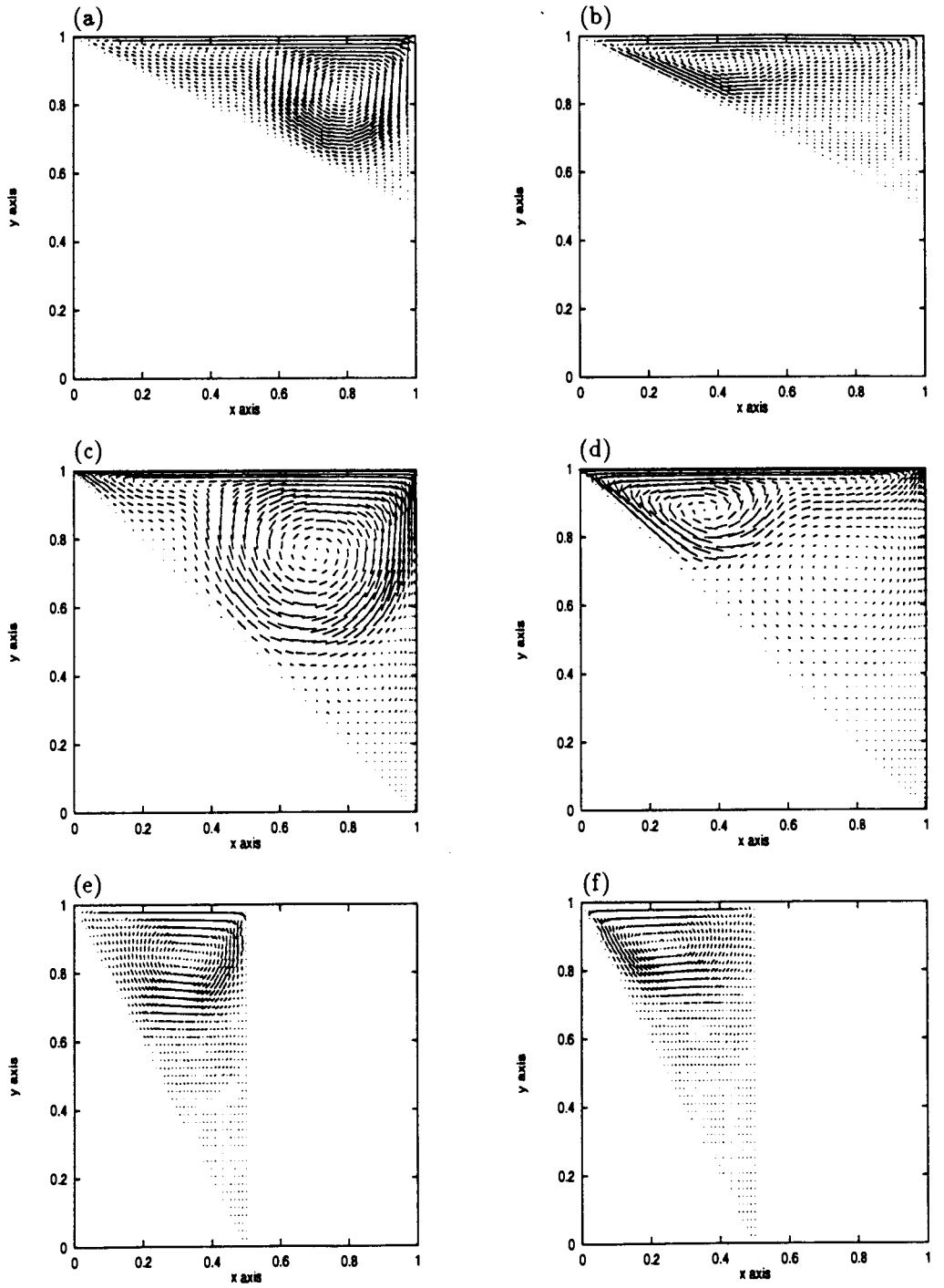

Figure 3.5: Transition of the shape pattern 4.
Wind goes to X-positive direction for the figures on the left and wind goes to X-negative direction for the figures on the right.

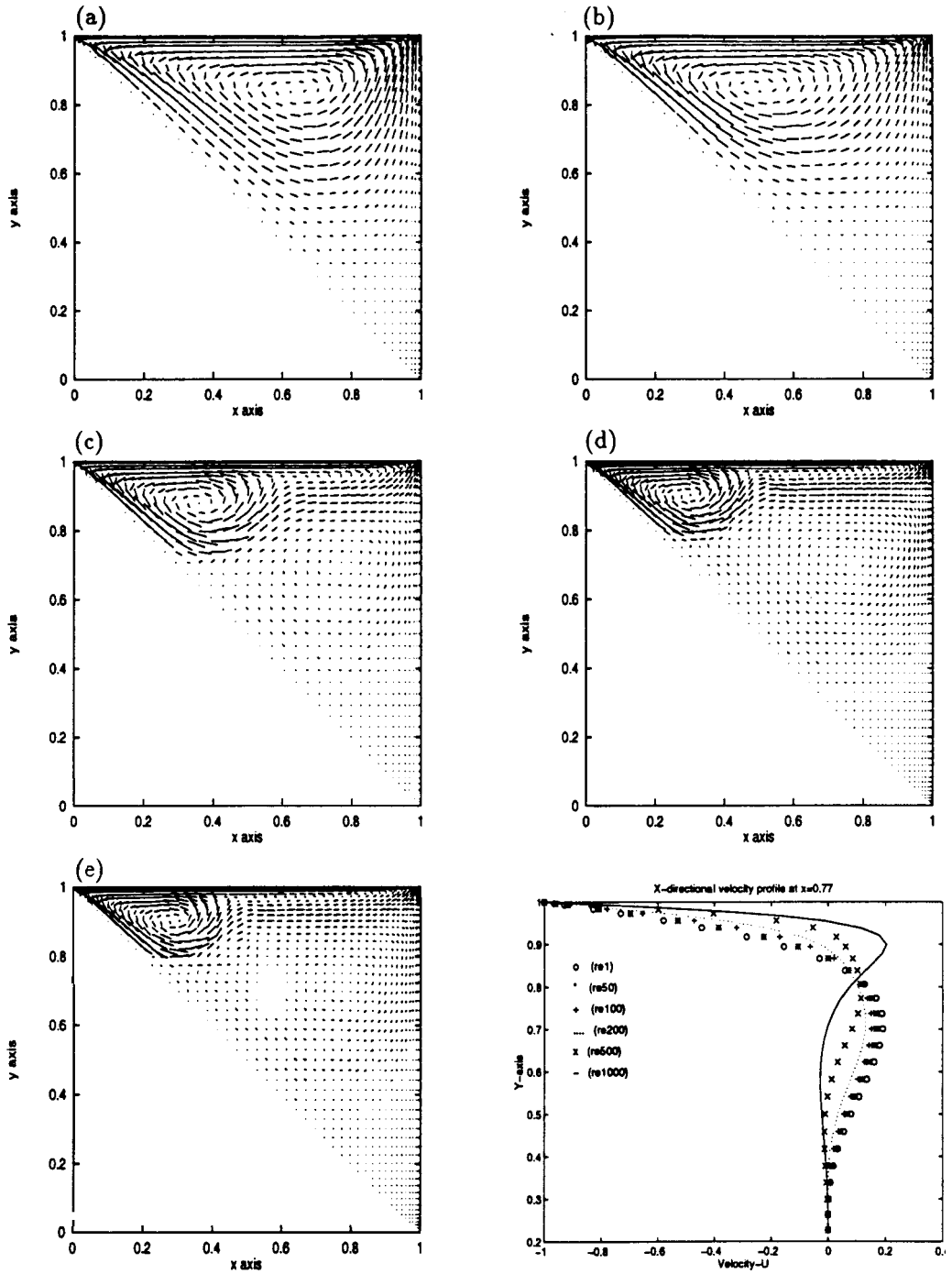

Figure 3.6: Steady state solutions with higher Reynolds numbers. (a)Re=1 (top left) (b)Re=200 (c)Re=1000 (d)Re=2000 (e)Re=3000 (bottom left). The figure at the bottom right conner is for x-directional velocity profiles at x≈0.77 with small Reynolds numbers.

Chapter 4

Time-dependent problems

Time dependent cavity problems are investigated for the isosceles right triangular domain. The second order accurate finite difference approximation is employed to discretize the time derivative terms. To observe the Hopf bifurcation, total kinetic energy is used as a global change indicator. Some oscillatory behavior is observed which may indicate a time periodic solution.

4.1 review of bifurcation problems

Since we are living in the world which is surrounded by a large quantity of fluid, any of our activities are influenced by it to some degree. When we are living our daily life in the pool of air, we consciously or unconsciously benefit from it as it refreshes and sustains our bodies. Air and water also help to accelerate a plane or ship and they play a major role in the reduction of fuel efficiency. In many cases, most of incidents involve constant dramatic changes in the qualitative structure of the fluid. Wind, the motion of the air, ceaselessly changes its strength and direction. Whirlpools which may appear near the non-smoothed body parts of a car, plane or ship constantly change shape and position as time elapses. In real life models, people are usually concerned about the long-time behavior of the solutions. In numerical

computation, this may give steady state solutions, periodic solutions and many other types of solutions. Most of the fluid phenomena observed by us in daily life are turbulent and have very high Reynolds numbers. On the other hand, most of the early researches in the fluid dynamics were about steady state problems. The potentially rich unsteady cavity dynamics have only recently begun to be addressed. Nowadays it is widely believed that the Navier-Stokes equations can model the complex natural fluid phenomena associated with the transition to turbulence. Hopf bifurcation theory or, more generally, bifurcation theory; which are popular in ODE, however, are quite rarely applied to Navier-Stokes equations. The reason is that an accurate simulation of a flow problem requires a very large number of degrees of freedom and a correct simulation of bifurcation phenomena is thus computationally expensive. Until now most of the bifurcations observed by researchers in fluid dynamics were of Hopf type. To detect and confirm a Hopf bifurcation, we need to setup some kinds of indicators. There are many ways to display the information which is obtained by taking any scalar value data as time proceeds. The most immediate way to display those data is to plot them against time. However, this type of presentation may hide the important features of information. The two most powerful indicators of the qualitative features of nonlinear dynamical systems are spectral densities and phase diagrams. A spectral density or power spectrum is a well-known device in the field of signal processing which identifies flow frequencies and their relative strength. A phase diagram or phase portrait is constructed by mapping values of scalar data at the same point but separated by multiples of a fundamental time delay T.

Shen [23, 24] reported Hopf bifurcation about a numerical simulation of unsteady incompressible flows in a unit cavity. He used a second order projection scheme proposed by Kim and Moin [30] in time and a Chebyshev-Tau approximation (spectral method) for the space variable. The boundary condition for the top lid is regularized [u = $(16x^2(1-x)^2, 0)$] to take advantage of the spectral accuracy. The first Hopf bifurcation is observed at Re=10500 and the other one at Re=15500. Since the effective Reynolds number of the flow with unsmoothed boundary conditions is larger than that of the flow with regularized boundary conditions, the nonsmooth driven

cavity flow will exhibit Hopf bifurcation with smaller Reynolds numbers. Bruneau and Jouron [25] observed transition to turbulence in the unit cavity flow for a Reynolds number lower than 7500 by solving the steady Navier-Stokes equations with a high resolution grid. The main measurements Shen used to identify the bifurcation are time historical velocity profile at some fixed point for a local indicator and total kinetic energy for a global indicator which is

$$E(n\Delta t) = \left\{ \sum_{i,j=0}^{N-1} \left[(u_{i,j}^n)^2 + (v_{i,j}^n)^2 \right] \right\}^{1/2}$$

where $u_{i,j}^n, v_{i,j}^n$ are the (i,j)th coefficients of the Chebyshev expansion of the two components of the velocity at the nth step. Fortin *et al* [27] observed the Hopf bifurcation to turbulence by solving the unsteady Navier-Stokes equations using a standard Galerkin approximation and a loading strategy for increasing the Reynolds number. The main measure they used to detect the bifurcations is the phase portraits of the velocities taken from the same point as time proceeds. They showed very odd figures which may called strange attractor. This is one of the very rare numerical simulations of chaotic behavior of Navier-Stokes equations. However, they could not confirm that the results are really true. Gustafson and Halasi [29] found a persistent oscillation in the study of the unsteady viscous incompressible flow in a higher aspect ratio (A=depth/width=2) driven cavity at a higher Reynolds number (Re=10,000). The Navier-Stokes equations are discretized on a uniform 40×80 grid using a modified MAC (marker and cell) staggered mesh scheme. They graphically showed an indication of a Hopf bifurcation by the time history of the velocity field. Goodrich *et al* [26] also studied a Hopf bifurcation of a driven cavity flow with an aspect ratio of two. Their numerical algorithm is based on the time dependent stream function equation, with a Crank-Nicolson differencing scheme for the diffusion terms, and with an Adams-Bashforth scheme for the convective terms. They reported a periodic solution at Re=10,000 on a coarse rectangular 48×96 mesh and two periodic solutions at Re=5000 on 48×96 and 96×192 grids. To determine the Hopf bifurcation they collected numerous useful measures to identify the final asymptotic state of cavity flows. We will briefly list the measures and indicators they used for the qualitative

representation of a flow structure.

(1) **Standard two-dimensional field representations**

- stream function contour plots
- stream function surface plots
- velocity vector plot
- kinetic energy contour plot
- kinetic energy surface plot
- vorticity contour plot
- vorticity surface plot
- pressure gradient vector plot.

These plots are multi-purpose and each one has its own characteristics. Among them the stream function contour plot, the velocity vector plot and the vorticity contour plot are the most commonly used representations.

(2) **Indicators of dynamics**

The following indicators are used for tracking convergence to an asymptotic state and for understanding the qualitative nature of that state. They are either mathematical norms or data at a fixed point. A mathematical norm can be a global indicator while point data value show a local behavior of flow.

- the relative L_1 norm of the stream function change per time step (global)

$$\frac{\sum_{i,j} \mid \psi_{i,j}^{n+1} - \psi_{i,j}^{n} \mid}{\sum_{i,j} \mid \psi_{i,j}^{n+1} \mid}$$

- the maximum and minimum stream function value

- the relative L_1 norm of the vector field change per time step (global)

$$\frac{\sum_{i,j}\left(\mid u_{i,j}^{n+1}-u_{i,j}^{n}\mid+\mid v_{i,j}^{n+1}-v_{i,j}^{n}\mid\right)}{\sum_{i,j}\left(\mid u_{i,j}^{n+1}\mid+\mid v_{i,j}^{n+1}\mid\right)}.$$

- the total kinetic energy

$$\frac{1}{2}\Delta x\Delta y\sum_{i,j}\|\mathbf{u}_{i,j}^{n+1}\|_2^2$$

- the maximum acceleration

$$\max\left\{\frac{\|\mathbf{u}_{i,j}^{n+1}-\mathbf{u}_{i,j}^{n}\|_2}{\Delta t}\right\}$$

- stream function value at a point
- velocity component at a point
- kinetic energy value at a point
- vorticity value at a point

They reported that the relative L_1 stream function change norm and the total kinetic energy are very good complements for indicating convergence to an asymptotic state.

Transition of the properties of a cavity flow to chaos is also reported on problems other than wind driven cavity flows. Paolucci and Chenoweth [32] investigated a Boussinesq fluid in two-dimensional closed, differentially heated vertical cavities. By changing the aspect ratio and Rayleigh number, they observed the flow transition to chaos. The main measurements they used to detect the bifurcations were the following: time history of temperature versus velocity components at fixed points; power spectrum of the fluctuating values of velocity versus temperature at fixed locations; and phase space trajectory of temperature versus velocity component u. They showed a clear characteristic properties of the Boussinesq flow.

Related to the topics of the chapter 3, square driven cavity flow or rectangular driven cavity flow with aspect ratio 2 is also used as a test model for the new

time dependent numerical scheme. Extension to the time dependent incompressible Navier-Stokes equations of the finite difference Galerkin (FDG) method was tested on the square and rectangular driven cavity flows by Goodrich and Soh [31]. Their method uses the fourth-order stream function equation with a Crank-Nicolson Adams-Bashforth algorithm to treat time derivative.

4.2 numerical results

As is reported in the references [23, 24, 29], unsmoothed driven cavity flows or cavity flows with a different shape of domain from a square will lead to a bifurcation with a considerably smaller Reynolds number than the regularized square cavity flow for which critical Re value is about 10500. From the experience of these calculations, the shape we used for the time dependent problem is the one that is the most difficult to increase Reynolds numbers. This led us to conjecture that we might be able to observe a bifurcation with a relatively small Reynolds number. The method we used is based on the same method used in the previous chapter.

As the Reynolds number increases, the qualitative change of flow becomes time sensitive. Then a time-accurate discretization scheme is necessary for simulating unsteady flows. The major difficulty in obtaining a time-accurate solution for an incompressible flow arises from the fact that the continuity equation does not contain a time-derivative explicitly. It can be shown that failure to preserve properties such as global conservation of momentum, kinetic energy or circulation can lead to numerical instabilities especially for high Reynolds numbers. For the discretization of the time derivative we used a Gear's scheme based on the approximation,

$$\partial \mathrm{u}/\partial t = (3\mathrm{u}^{\mathbf{n+1}} - 4\mathrm{u}^{\mathbf{n}} + \mathrm{u}^{\mathbf{n-1}})/2\Delta t + \theta(\Delta t^2). \tag{4.1}$$

This second order accurate two-step method is known to be stiff stable. All zero velocity values and the steady state solution with Re=3400 are used as initial data. The main measure we used to determine whether a flow had attained its final asymptotic

state was the total kinetic energy (TKE):

$$\left[\int\int_{\Omega}\left(u^2+v^2\right)d\Omega\right]^{1/2} \tag{4.2}$$

where u and v are the two components of the velocity of each node at each nth time step. And they are summed up over the whole domain. Here we used a fixed time step Δt=0.05.

Let us see the first plot (t=2) of Figure 4.1 which starts with its initial data at zero. The primary eddy has been already formed at the top left corner, which is more compact than that of Re=3,400, but the secondary eddy has not appeared yet. At t=4 and t=6, the secondary eddy, generated by the main eddy, begins to form. Then it moves toward the upstream and is separated from the primary eddy. At t=16, the secondary eddy is fully developed and occupied a large area. Also, there is some turbulence or a tertiary eddy appearing between the first and the second eddies. At t=18, the turbulence is almost settled. This point corresponds approximately to the local minimum total kinetic energy as we shown in Figure 4.3. The figure at t=20 is quite similar to that at t=16 and takes about the same total kinetic energy which is almost the local maximum value of the Figure 4.3.

The time history of the kinetic energy of the solution is presented in Figure 4.3. From the graph we can recognize that the oscillation is clearly formulated with approximately the same amplitude after the third peak (t$\approx$12). For reference, we also show the time history profile of the total kinetic energy with Re=2000 in Figure 4.2 which has a steady state solution. Again, due to the restriction of time we only calculated up to t=20. Comparing Figure 4.2 with Figure 4.3, we can recognize qualitative differences: the size of the oscillation in Figure 4.2 is gradually suppressed and becomes smaller while those in Figure 4.3 is sustained.

To ensure that the oscillation in Figure 4.3 persists, we also calculated the same flow problem with the steady state solution with Re=3400 as its initial value (see Figure 4.4). The 4.4-(a) is the steady solution with Re=3400 and is used as the initial data for the rest of the calculations. As we can observe from the figures (b) to (f), the flow is repeatedly changing its pattern. Roughly speaking, the figures (b), (d) and (f) are qualitatively similar and they approximately corresponds to the local minimum values of Figure 4.5. On the other hand, figures (c) and (e) are graphically similar to each other and roughly correspond to the local maximum values seen in Figure 4.5. The amplitudes of waves in Figure 4.5 after t=15 are ranging from 0.011562 to 0.011624 (left side peak minus right side peak), which are very close to those of Figure 4.4. In addition the wavelengths are either 3.85 or 3.95 which are exactly the same as those in Figure 4.3. Overall we observe that the velocity vector field pattern at the beginning of the cycle is almost perfectly recaptured at the end of the cycle. This strongly indicates the global periodic feature of the solution in the entire domain. In the figure 4.5 the periodic oscillation still remains without a substantial reduction of the amplitude. Because of the fairly limited power of computer speed and time, the approximate solutions presented here were not fully developed into a final asymptotic state and thus we can not conclude whether this oscillatory result is really a periodic one or will eventually disappear.

Figure 4.6 shows the phase portraits of the total kinetic energy versus the total kinetic energy with time delay t=2.5 for the figure on the left and t=3.5 for the figure on the right. The data used are based on the same data used for the 4.5(b) of Figure 4.5. Although the trajectories in both figures are not closed and are shifting, the basic shape and size of the trajectories seem to be preserved.

From these calculations we found that the approximate solution quickly developed into a time periodic pattern, although it probably needs a very long time for the solution to attain its final asymptotic periodic state. Together with the facts we considered previously, we thus have some confidence that the oscillation will remain and may be able to call this phenomena a Hopf bifurcation. Although in order to verify the legitimacy of the results we have to use a much finer grid with possibly

a smaller time step for the same problem and ascertain that a qualitatively similar solution is produced. That would be far above the capability of our computers, and thus remains a future topic.

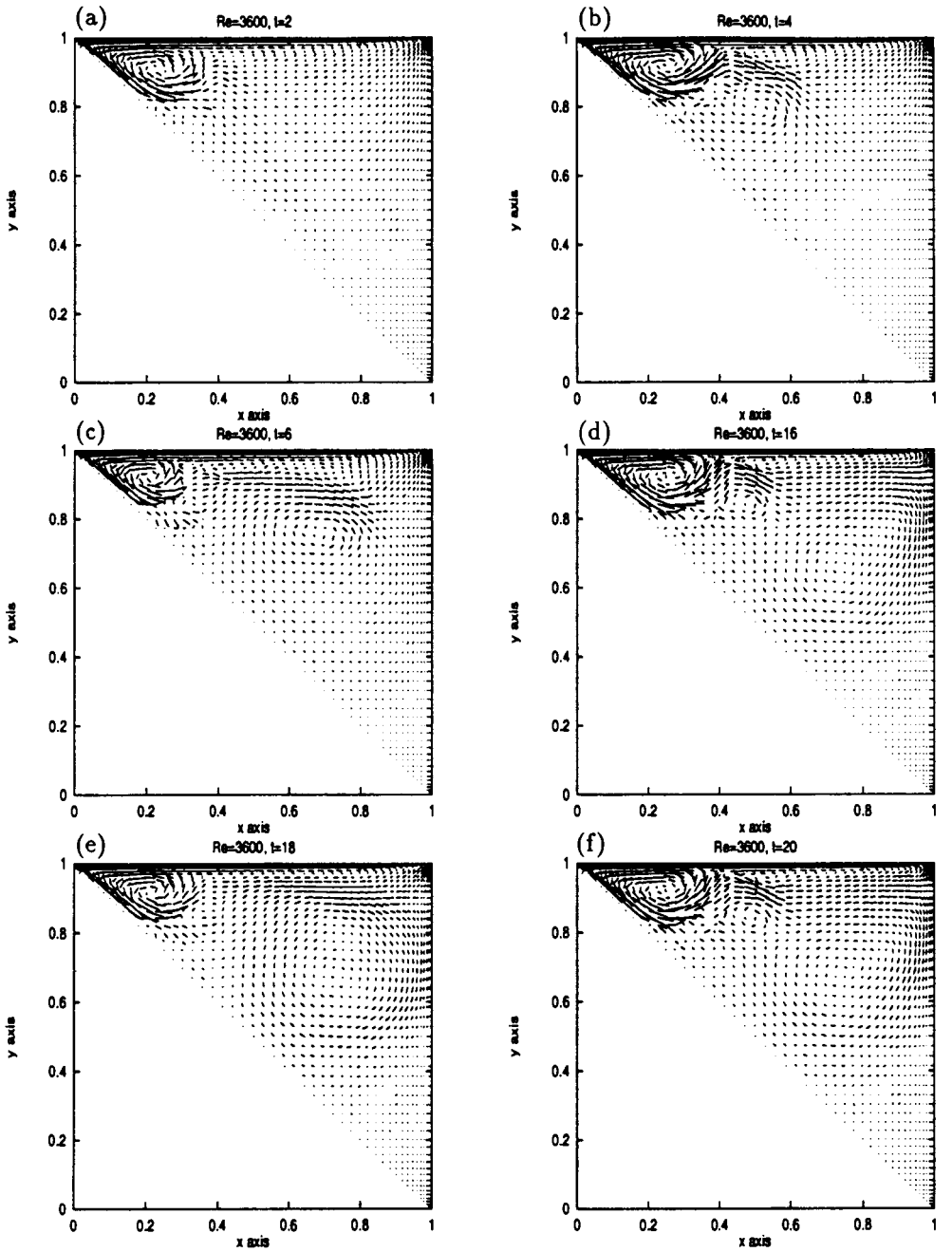

Figure 4.1: Unsteady problem with all-zero I.C.
Re=3600 and Δt=0.05: (a) t=2 (top left), (b) t=4, (c) t=6, (d) t=16, (e) t=18, (f) t=20.

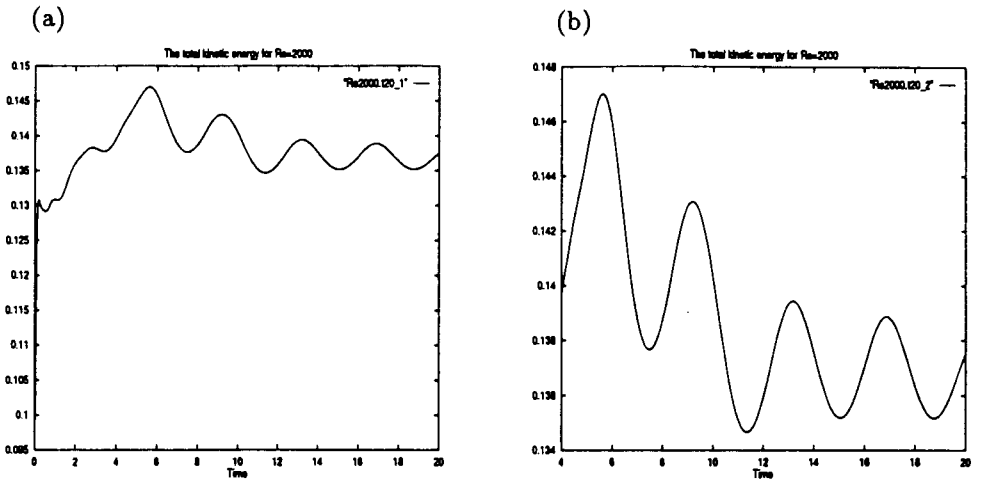

Figure 4.2: The total kinetic energy 1.
45×45 grid (1035 points) with Re=2000, Δt=0.05.

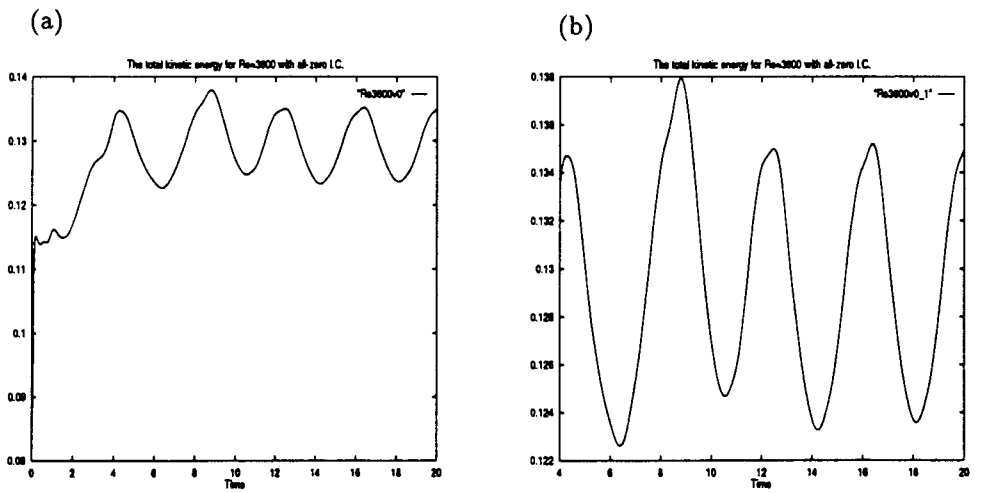

Figure 4.3: The total kinetic energy 2.
55×55 grid (1540 points) with Re=3600 and Δt=0.05.
Initial data are set to be all zero.

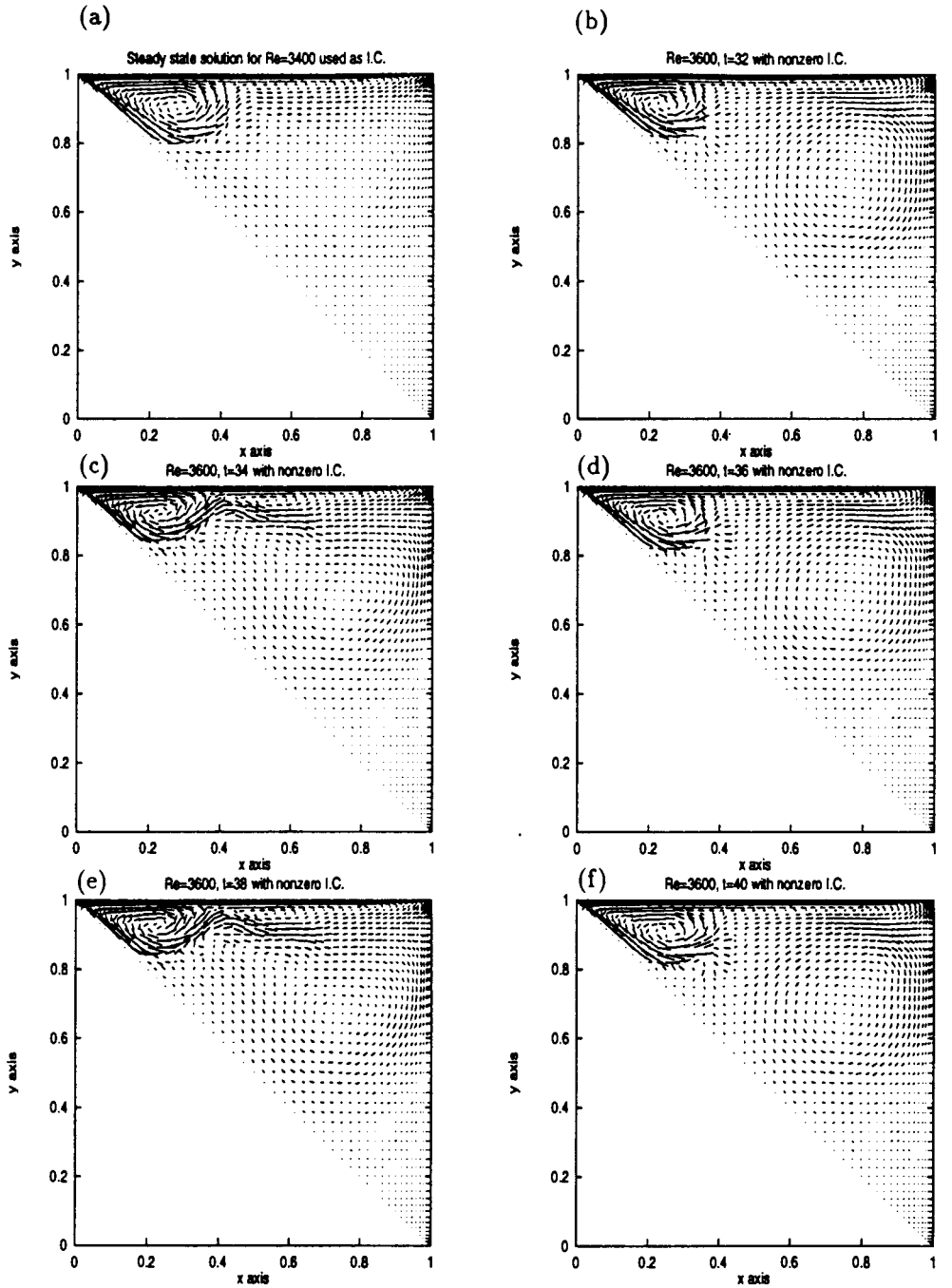

Figure 4.4: Unsteady problem with non-zero I.C.
Re=3600 except for the first figure which is used as initial data.
Δt=0.05 and (a) t=0 (top left), (b) t=32, (c) t=34, (d) t=36, (e) t=38, (f) t=40.

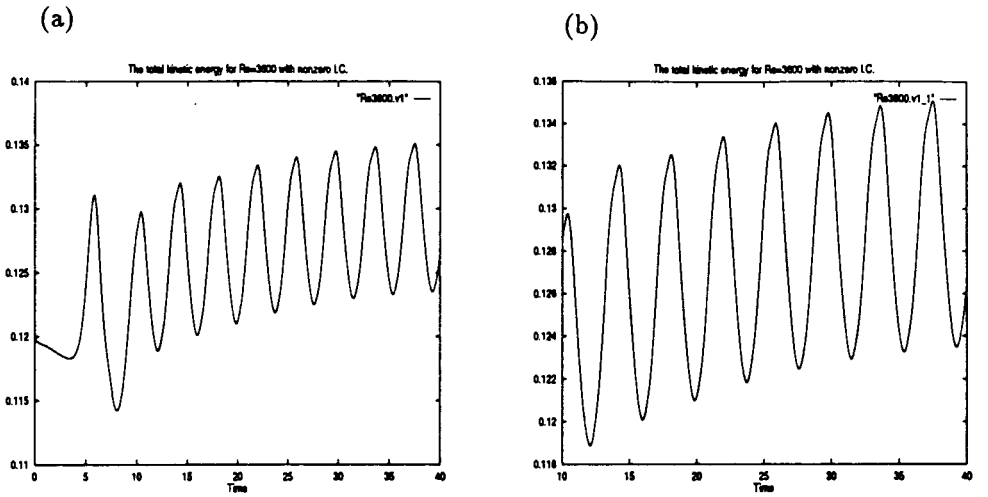

Figure 4.5: The total kinetic energy 3.
55×55 grid (1540 points) with Re=3600. Δt=0.05.
Steady state solution with Re=3600 is used as the initial data.

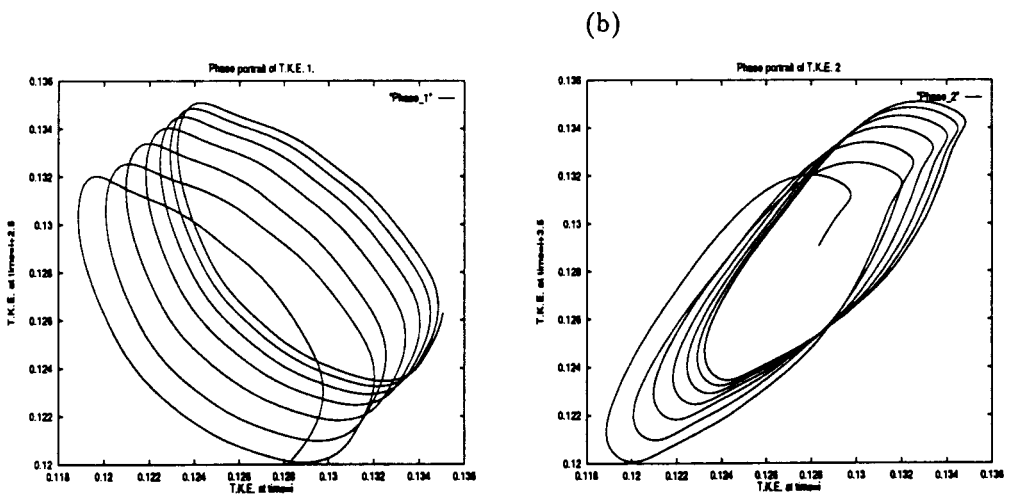

Figure 4.6: The phase portrait.
The total kinetic energy versus the total kinetic energy with time delay 2.5 for the left and 3.5 for the right.

Chapter 5

Discussion of validity

As is mentioned in [33], Bezout's theorem assures us that an algebraic system with N unknowns has essentially 2^N solutions. In case of an $N \times N$ two dimensional grid problem, the system has 2^{N^2} numerical solutions. Therefore if the problem to be solved has a unique solution, we might have one of the $2^{N^2} - 1$ spurious solutions unless the solution is close enough to the true solution. Fortunately most of the computational solutions are complex and we do not usually end up with them by means of real numerical calculations. But this is not always the case. In [33] Schreiber and Keller showed that even time marching schemes may lead to spurious steady states. Unfortunately there is no good theory to determine whether the approximated solution is spurious or legitimate. For the validity of the numerically obtained results we have to check them against the known experimental results or recalculate the same problem with a finer grid to obtain the essentially same results. Because of the restriction of both computational power and time, we used rather coarse meshes for most of the computation. However as we will show later, they still hold most of the properties of the results obtained by using much finer mesh. In the examples of the steady state problems, the Reynolds number is fixed to 1,000 and the figures with coarse meshes are the same as shown in chapter 3.

For the calculation of a square cavity with finer mesh we used a 59×59 non uniform grid (Figure 5.1), by which the solution of the right upper corner has been much

improved and smoothed. In general, there is a dominant recirculating eddy generated by the moving wall and two smaller counter-rotating eddies at the bottom stagnant corners. The graphically obtained center of the eddy with coarse mesh is (0.529,0.560) which seems to be satisfactorily close to that with a finer mesh's (0.531,0.571). For the calculation of Figure 5.2, we used 55×55 grid (1540 points) for right hand side finer mesh and the same mesh as given in chapter 3 for the left hand side coarser mesh. Again, clearly the two figures are qualitatively almost identical except for the exact position of the primary and secondary vortices. Because of the concentration of the grid at the corner, the situation of the corner velocity is much more acceptable than the above square cavity case. The approximated center of the primary eddy for the coarser mesh is (0.360,0.875) and (0.372,0.864) for finer one.

Figure 5.3 shows typical examples of Hopf bifurcation plots which are taken from the paper by Shen [23]. As mentioned in chapter 4, due to the lack of computational time and power, we could not continue to run the program until it reached the final asymptotic state. However, our calculation exhibits the basic behavior of a bifurcation. As in Figure 4.3 or 4.5, obtained plots are periodic in time with an almost fixed interval, approximately the same minimum and maximum values and a similar shape pattern. Those facts enable us to believe that our calculations are fairly reliable.

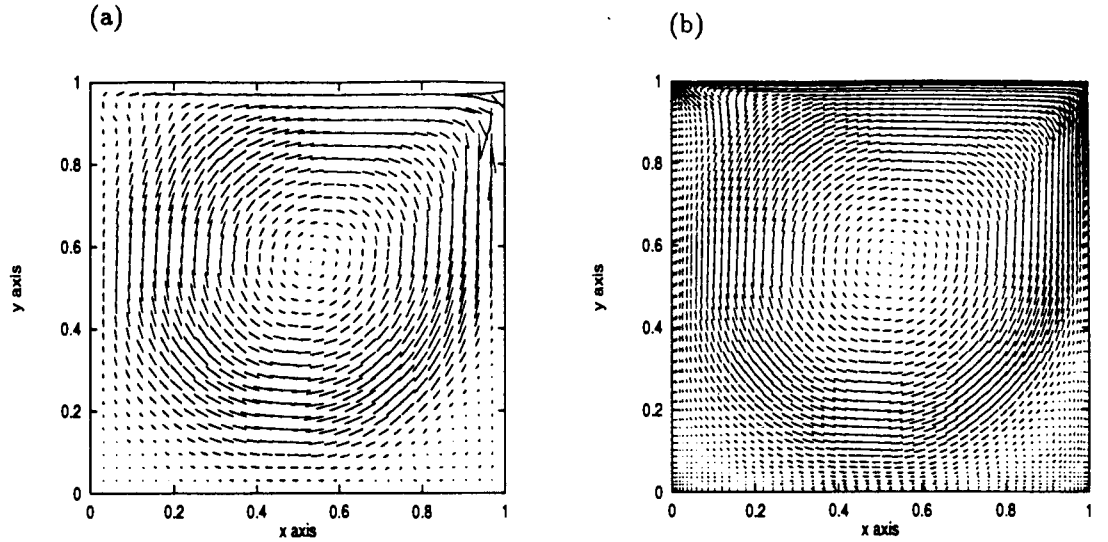

Figure 5.1: The square cavity flows with two different grids.
33×33 grid (1089 points) for (a)
59×59 grid (3481 points) for (b)

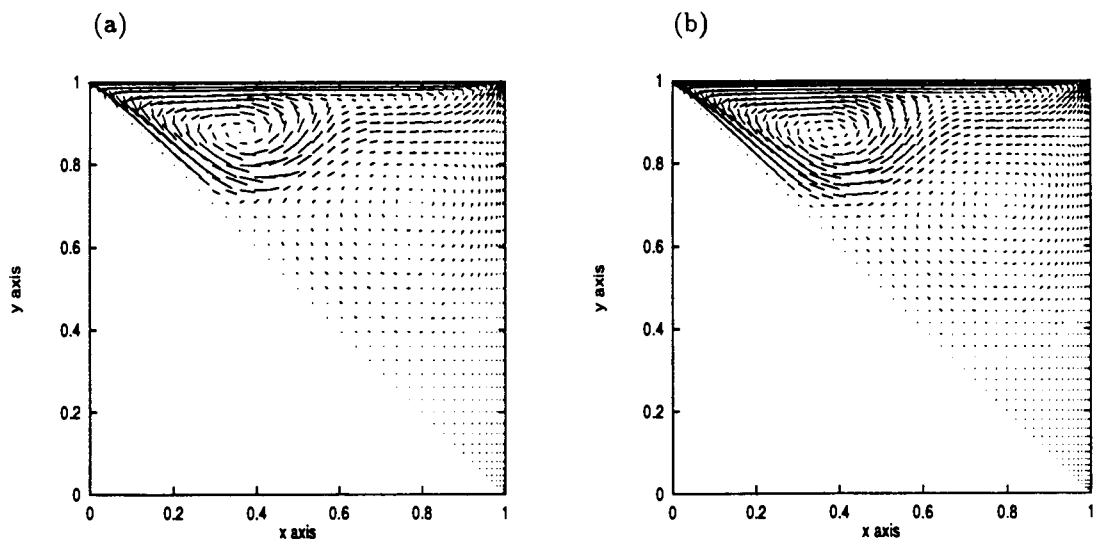

Figure 5.2: The right triangular cavity flows with two different grids.
45×45 grid (1035 points) for (a)
55×55 grid (1540 points) for (b)

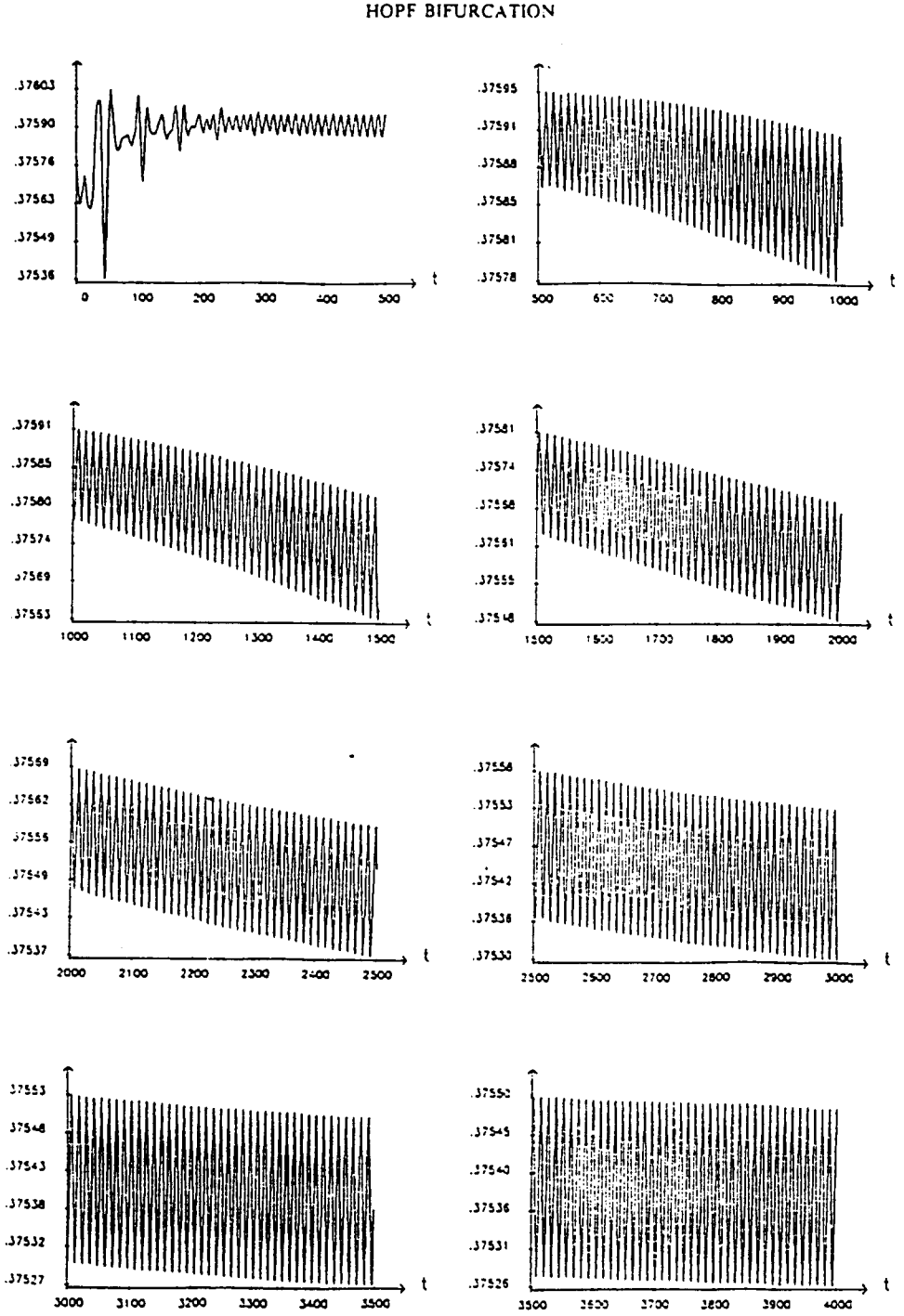

FIG. 4. Convergence histories of kinetic energy of the flow at Re = 10,500 with 49 × 49 modes.

Figure 5.3: Typical example of a Hopf bifurcation.
Duplicated from the paper [23].
It will reach its asymptotic periodic state at about t=4500.

Chapter 6

Conclusion and discussion

We have investigated the effect of the change of a shape to the qualitative and the quantitative features of cavity flows. Several patterns have been considered and it was found that the flow structures are sensitive to shape differences. The size of eddies is greatly influenced by the angle of a downstream corner. The difficulty of increasing Reynolds numbers also differs with each shape. We found that the shape we used for time dependent problems is one of the hardest to converge. This shape has been further investigated with higher Reynolds numbers. Although the standard application of the finite difference method fails to give a well-posed system for some shapes (it was briefly presented in chapter 3), as expected, our standard formulation of FEM works well with little difficulty for all shapes. We could easily increase a Reynolds number with a fairly small number of unknowns.

For the time-dependent problem, we have used two different initial conditions; all-zero velocity components and the steady state solution with Re=3400. The former one is used to see the flow dynamics itself and the time needed for it to develop bifurcation. The latter one is used to possibly see the long time behavior of the solution. In this thesis we used the total kinetic energy plot, velocity vector field plot and phase portrait of the total kinetic energy to observe a global phenomenon of a bifurcation since we do not know, in advance, whether this phenomenon is only local or global. We thus did not attempt to choose a specific point for the local indicator

which may hide a global behavior of a flow.

As in Figures 4.3 and 4.5, the results obtained from the two different initial conditions exhibit quite similar behaviors which also resemble published results of a Hopf bifurcation (see such as [23]). Finally we will provide some possibilities for further investigation which are the natural extension of this thesis.

For the steady state problems:

- Since we can consider many more shape transformation patterns, we can also investigate the same things for other patterns.
- For a fixed Reynolds number, starting from a periodic solution, change the shape slightly to obtain a steady state solution or other bifurcations , or vice versa. (Since in practice turbulence is generally unpreferable, this may have an industrial application.)

For the time dependent problems:

- Further increase the Reynolds number with a much finer grid and observe other bifurcations and hopefully chaos.
- Identify the specific critical values to the Hopf bifurcation for each shape and study the effect of the change of a shape.

All of above future topics probably require much more computational resources including a super computer, and are burdensome for today's mainframe, but will be practicable in the near future.

Bibliography

[1] C. Cuvelier, A. Segal and A. A. V. Steenhoven, 1986 *Finite Element Methods and Navier-Stokes Equations*, D.Reidel Publishing Company, Dordrecht/Boston/Lancaster/Tokyo.

[2] O. C. Zienkiewicz and R. L. Taylor, 1989 *The Finite Element Method 4th ed.* (Volume 1 Basic Formulation and Linear Problems), McGraw-Hill Book Company, London.

[3] G Dhatt and G Touzot, 1984 *The Finite Element Method Displayed*, John Wiley & Sons, Chichester/New York/Brisbane/Toront/Singapore.

[4] J. E. Akin, 1994 *Finite Elements Analysis and Design*, Academic Press Harcourt Brace & Company, London/SanDiego/New York

[5] C. A. J. Fletcher, 1988 *Computational Techniques for Fluid Dynamics* (Volume 1 Fundamental and General Techniques), Springer-Verlag, Berlin/Heidelberg/New york/London

[6] R. L. Burden and J. D. Faires, 1989 *Numerical Analysis 4th ed.*, Pws-Kent Publishing Company, Boston/Massachusetts

[7] P. C. Hammer, O. P. Marlowe and A. H. Stroud, 1956 'Numerical Integration over Simplexes and corns', *Math. Tables Aids Comput.* **10**, 130-137

[8] R. Glowinski and O. Pironneau, 1979 'On a Mixed Finite Element Approximation of the Stokes Problem (I)', *Numer. Math.* **13**, 397-424

[9] M. Bercovier and O. Pironneau, 1979 'Error Estimates for Finite Element Method Solution of the Stokes Problem in the Primitive Variables', *Numer. Math.* **13**, 211-224

[10] C. J. Ribbens and L. T. Watson, 1994 'Steady Viscous Flow in a Triangular Cavity', *Comput. Phys.* **112**, No.1, 173-181

[11] W. D. McQuan, C. J. Ribbens, C. Y. Wang and L. T. Watson, 1994 'Steady Viscous Flow in a Trapezoidal Cavity', *Comput. Fluids* **23**, No.4, 613-626.

[12] M. Li and T. Tang, 1994 'Steady Viscous Flow in a Triangular Cavity by Efficient Numerical Techniques', *S.F.U. research report No.94-09.*

[13] S. Y. Tuann and M. D. Olson, 1978 'Review of Computing Methods for Recirculating Flows', *J. Comput. Phys.* **29**, 1-19

[14] R. Schreiber and H.B.Keller, 1983 'Driven Cavity Flows by Efficient Numerical Techniques', *J. Comput. Phys.* **49**, 310-333

[15] K. Gustafson and K. Halasi, 1986 'Vortex Dynamics of Cavity Flows' *J. Comput. Phys.* **64**, 279-319

[16] R. L. Quere and T. A. de RoQuefort, 1985 'Computation of Natural Convection in Two-Dimensional Cavities with Chebyshev Polynomials' *J. Comput. Phys.* **57**, 210-228

[17] E. M. Sparrow and M. Charmchi, 1980 'Heat Transfer and Fluid Flow Characteristics of Spanwise-Periodic Corrugated Ducts' *Int. J. Mass Transfer* **23**, 471-481

[18] C. N. Savvides and J. H. Gerrard, 1984 'Numerical Analysis of the Flow through a Corrugated Tube with Application to Arterial Prostheses' *J. Fluid Mech.* **138**, 129-160

[19] A. Mayo and A. Greenbaum, 1992 'Fast Parallel Iterative Solution of Poisson's and the Biharmonic Equations on Irregulor Regions' *SIAM J. Sci. Statist. Comput.* **13**, 101-118

[20] R. J. Leveque and Z. Li, 1994 'The Immersed Interface Method for Elliptic Equations with Discontinuous Coefficients and Singular Sources' *SIAM J. Numer. Anal.* **31**, 1019-1044

[21] Engelman, G. Strang and K. J. Bathe, 1981 'The Application of Quasi-Newton Methods in Fluid Mechanics' *Int. J. Num. Meth. Engng.* **17**, 707-718

[22] G. K. Batchelor,1956 'On Steady Laminar Flow with Closed Streamlines at Large Reynolds Number' *J. Fluid Mech.* **1**, 177-

[23] J. Shen, 1991 'Hopf Bifurcation of the Unsteady Regularized Driven Cavity Flow', *J. Comput. Phys.* **95**, 228-245.

[24] J. Shen, 1990 'Numerical Simulation of the Regularized Driven Cavity Flows at High Raynolds Nombers', *Comput. Meth. Appl. Mech. Eng.* **80**, 273-80.

[25] C. H. Bruneau and C. Jouron, 1988 'Un nouveau schéma décentré pourle problème de cavité entrainée', *C. R. Acad.Sci. Paris* **307**, 359-362.

[26] J. W. Goodrich, Gustafson and Halasi, 1990 'Hopf Bifurcation in the Driven Cavity', *J. Comput. Phys.* **90**, 219-261.

[27] A. Fortin, M. Fortin and J. J. Gervais, 1987 'A Numerical Simulation of the Transition to Turbulence in a Two-Dimensional Flow', *J. Comput. Phys.* **70**, 295-310.

[28] U. Ghia, K. N. Ghia and C. T. Shin, 1982 'High Re Solutions for Incompressible Flow Using the Navier-Stokes Equations and a Multigrid Method', *J. Comput. Phys.* **48**, 387-411.

[29] K. Gustafson and Halasi, 1987 'Cavity Flow Dynamics at Higher Reynolds Number and Higher Aspect Ratio', *J. Comput. Phys.* **70**, 271-283.

[30] J. Kim and P. Moin, 1985 'Application of a Fractional-Step Method to Incompressible Navier-Stokes Equations', *J. Comput. Phys.* **59**, 308-323.

[31] J. W. Goodrich and W. Y. Soh, 1989 'Time-Dependent Viscous Incompressible Navier-Stokes Equations: The Finite Difference Galerkin Formulation and Streamfunction Algorithms' *J. Comput. Phys.* **84**, 207-241

[32] S. Paolucci and D. R. Chenoweth, 1989 'Transition to Chaos in a differentially heated vertical cavity' *J. Fluid Mech.* **201**, 379-410

[33] R. Schreiber and H. B. Keller, 1983 'Spurious Solutions in Driven Cavity Calculations' *J. Comput. Phys.* **49**, 165-172

[34] J. G. Heywood and R. Rannacher, 1982 'Finite element approximation of the nonstationary Navier-Stokes problem. 1: Regularity of Solutions and Second-Order Error Estimates for Spatial Discretization' *SIAM J. Numer. Annal.* **19**, 275-312

[35] J. G. Heywood and R. Rannacher, 1986 'Finite element approximation of the nonstationary Navier-Stokes problem. part 2: Stability of Solutions and Error Estimates Uniform in Time' *SIAM J. Numer. Annal.* **23**, 750-777

[36] J. G. Heywood and R. Rannacher, 1988 'Finite element approximation of the nonstationary Navier-Stokes problem, part 3: Smoothing Property and Higher Order Error Estimates for Spatial Discretization' *SIAM J. Numer. Annal.* **25**, 480-503